

# Entropy-based viscous regularization for the multi-dimensional Euler equations in low-Mach and transonic flows

Marc O. Delchini<sup>a</sup>, Jean C. Ragusa<sup>\*,a</sup>, Ray A. Berry<sup>b</sup>

<sup>a</sup>*Department of Nuclear Engineering, Texas A&M University, College Station, TX 77843, USA*

<sup>b</sup>*Idaho National Laboratory, Idaho Falls, ID 83415, USA*

---

## Abstract

We present a new version of the entropy viscosity method, a viscous regularization technique for hyperbolic conservation laws, that is well-suited to low-Mach flows. By means of a low-Mach asymptotic study, new expressions for the entropy viscosity coefficients are derived. These definitions are valid for a wide range of Mach numbers, from subsonic flows (with very low Mach numbers) to supersonic flows, and no longer depend on an analytical expression for the entropy function. In addition, the entropy viscosity method is extended to Euler equations with variable area for nozzle flow problems. The effectiveness of the method is demonstrated using various 1-D and 2-D benchmark tests: flow in a converging-diverging nozzle; Leblanc shock tube; slow moving shock; strong shock for liquid phase; low-Mach flows around a cylinder and over a circular hump; and supersonic flow in a compression corner. Convergence studies are performed for both smooth solutions and solutions with shocks present.

*Key words:* entropy viscosity method, artificial viscosity, low-Mach regime, shock capturing, Euler equations with variable area.

---

## 1. Introduction

Solving accurately compressible fluid equations in the low-Mach limit is an ongoing topic of research. In many engineering applications, compressibility effects require the solution of the compressible fluid equations in nearly incompressible regimes and/or for low-Mach flow problems. For example, such flows are encountered in aerodynamics in the study of airships. In the nuclear industry, flows are nearly in the incompressible regime but compressible effects cannot be neglected because of the intense heat source, and because of some

---

\*Corresponding author

*Email addresses:* `delchmo@tamu.edu` (Marc O. Delchini), `jean.ragusa@tamu.edu` (Jean C. Ragusa), `ray.berry@inl.gov` (Ray A. Berry)

9 postulated accident scenarios, and thus need to be accurately resolved. Hence,  
10 there is a strong interest to develop computational methods that can solve both  
11 compressible and incompressible flow problems.

12 When solving Euler equations for a wide range of Mach numbers, multiple  
13 questions must be addressed: stability, accuracy and solution convergence in the  
14 low-Mach regime. Because of the hyperbolic nature of the equations, shocks can  
15 form during transonic and supersonic flows and require the use of adequate nu-  
16 merical techniques to stabilize solution and correctly resolve the discontinuities.  
17 A wide range of stabilization methods are available in the literature: approxi-  
18 mate Riemann solvers [18], flux-limiter techniques [3, 4], pressure-based viscosity  
19 methods [5], Lapidus method [6, 7, 8], and the entropy-viscosity method [1, 2],  
20 among others. These numerical methods are usually developed using simple  
21 equations of state and tested for transonic and supersonic flows where the dis-  
22 parity between the acoustic wave speed and the fluid speed is not excessively  
23 large and thus the Mach number is of order one. This approach, however, leads  
24 to a well-known accuracy problem in the low-Mach regime where the fluid ve-  
25 locity is smaller than the speed of sound by multiple orders of magnitude. The  
26 numerical dissipative terms become ill-scaled in the low-Mach regime and lead  
27 to the wrong numerical solution by changing the nature of the equations solved.  
28 This behavior is well documented in the literature [9, 10, 11]. In [9], a low-Mach  
29 asymptotic study has demonstrated convergence of the compressible Euler equa-  
30 tions to the incompressible ones. Many well-known stabilization techniques, for  
31 instance, the Roe scheme and the SUPG technique, do not yield the correct  
32 solution in the low-Mach regime and suitable modifications have been proposed  
33 (see [12] for the Roe scheme and [11] for the SUPG method). to ensure the  
34 convergence to the correct solution while preserving the original shock stabi-  
35 lization properties of these schemes. Additionally, the time step size may be  
36 severely restricted when solving compressible fluid equations with an explicit  
37 time discretization because of the large disparity between the fluid velocity and  
38 the speed of sound. To avoid an excessive number of explicit time steps, time  
39 preconditioners have been proposed and proved efficient [10]; however, because  
40 they modify the time derivatives in the governing equations, such acceleration  
41 techniques can only be used to obtain steady-state solutions for low-Mach flows  
42 using explicit schemes. To avoid modifying the time derivatives, the temporal  
43 implicit capabilities of the MOOSE multiphysics framework [13] are used. With  
44 such a choice, low-Mach steady-state solutions can be obtained effectively while  
45 preserving the accuracy of the transient solution; however, it requires the use of  
46 nonlinear solvers.

47 In this paper, we employ the entropy viscosity method as a numerical sta-  
48 bilization for the inviscid Euler equation and assess its performance in the low-  
49 Mach regime. The entropy viscosity method is a viscous regularization technique  
50 introduced by Guermond et al. to solve hyperbolic systems of equations and  
51 has successfully been applied to multi-dimensional supersonic flows with various  
52 spatial discretization schemes [14]. It is fairly straightforward to implement, can  
53 be used with unstructured grids, and has dissipative terms that are consistent  
54 with the entropy minimum principle. However, it has not been evaluated in the

low-Mach regime.

This paper is organized as follows: in Section 2 the current definition of the entropy viscosity method is recalled and its ill-scaled nature in the low-Mach regime is discussed. In Section 3, a new formulation of the viscosity residual is derived. This formulation no longer requires an analytical expression for the entropy function. A low-Mach asymptotic study is carried out to adapt the definition of the entropy viscosity coefficients in the incompressible limit while ensuring that the viscosity coefficients scale appropriately for all flow speeds (from low-Mach to supersonic). In Section 4, we extend the entropy viscosity method to Euler equations with variable area in order to model nozzle flows: the viscous dissipative terms are adapted so that the entropy minimum principle remains satisfied. Spatial and temporal discretizations and solution techniques are presented in Section 5. 1-D and 2-D numerical results are provided in Section 6 for a wide range of Mach numbers: liquid and gas nozzle flow problems, low-Mach flows over a cylinder and a circular bump (with Mach numbers as low as  $10^{-7}$ ), and supersonic flows in a compression corner [15]. Convergence studies are performed in 1-D in order to demonstrate the accuracy of the solution technique.

## 2. The Entropy Viscosity Method

### 2.1. Background

Euler equations in conservative form are given by

$$\partial_t \rho + \vec{\nabla} \cdot (\rho \vec{u}) = 0 \quad (1a)$$

$$\partial_t (\rho \vec{u}) + \vec{\nabla} \cdot (\rho \vec{u} \otimes \vec{u} + P \mathbb{I}) = 0 \quad (1b)$$

$$\partial_t (\rho E) + \vec{\nabla} \cdot [\vec{u} (\rho E + P)] = 0 \quad (1c)$$

where  $\rho$ ,  $\rho \vec{u}$  and  $\rho E$  are the density, the momentum and the total specific energy, respectively, and will be referred to as the conservative variables.  $\vec{u}$  is the fluid velocity and its specific internal energy is denoted by  $e = E - \frac{u^2}{2}$ . An equation of state, dependent upon  $\rho$  and  $e$ , is used to compute the pressure  $P$ . The tensor product  $\vec{a} \otimes \vec{b}$  is such that  $(\vec{a} \otimes \vec{b})_{i,j} = a_i b_j$ . The identity tensor is denoted by  $\mathbb{I}$ .

Next, the entropy viscosity method [1, 2, 16, 17] applied to Eq. (1) is recalled. The method consists of adding dissipative terms with a viscosity coefficient modulated by the entropy production; this allows for a high-order accuracy when the solution is smooth (provided that the spatial and temporal discretizations also are high order). The derivation of the viscous regularization (or dissipative terms) is carried out to be consistent with the entropy minimum principle; details and proofs of the derivation can be found in [14]. The viscous regularization thus obtained is valid for any equation of state as long as the physical entropy function  $s$  is concave (or  $-s$  is a convex function) with respect to the internal energy  $e$  and the specific volume  $1/\rho$ . The Euler equations with viscous regularization become

$$\partial_t \rho + \vec{\nabla} \cdot (\rho \vec{u}) = \vec{\nabla} \cdot (\kappa \vec{\nabla} \rho) \quad (2a)$$

94

$$\partial_t (\rho \vec{u}) + \vec{\nabla} \cdot (\rho \vec{u} \otimes \vec{u} + P \mathbb{I}) = \vec{\nabla} \cdot (\mu \rho \vec{\nabla}^s \vec{u} + \kappa \vec{u} \otimes \vec{\nabla} \rho) \quad (2b)$$

95

$$\partial_t (\rho E) + \vec{\nabla} \cdot [\vec{u} (\rho E + P)] = \vec{\nabla} \cdot \left( \kappa \vec{\nabla} (\rho e) + \frac{1}{2} \|\vec{u}\|^2 \kappa \vec{\nabla} \rho + \rho \mu \vec{u} \vec{\nabla} \vec{u} \right) \quad (2c)$$

96 where  $\kappa$  and  $\mu$  are positive viscosity coefficients (in units of  $\text{length}^2/\text{time}$ ).  $\vec{\nabla}^s \vec{u}$   
 97 denotes the symmetric gradient operator and guarantees the method to be ro-  
 98 tationally invariant [14]. The viscosity coefficients are key ingredients in the  
 99 viscous regularization of Eq. (2). Other stabilization approaches have been pro-  
 100 posed in the literature, for instance, the Lapidus method [8, 6] or pressure-based  
 101 viscosity methods [5]. Here, we follow the work of Guermond et al. and define  
 102 the viscosity coefficients,  $\kappa$  and  $\mu$ , based on the local entropy production. These  
 103 coefficients are numerically evaluated using the local entropy residual  $R_{\text{ent}}(\vec{r}, t)$   
 104 defined in Eq. (3);  $R_{\text{ent}}(\vec{r}, t)$  is known to be peaked in shocks and vanishingly  
 105 small elsewhere [18].

$$R_{\text{ent}}(\vec{r}, t) := \partial_t s + \vec{u} \cdot \vec{\nabla} s \quad (3)$$

106 In the current version of the method, the ratio of  $\kappa$  to  $\mu$  is defined through  
 107 a numerical Prandtl number,  $\text{Pr} = \kappa/\mu$ .  $\text{Pr}$  is a user-defined parameter and  
 108 is usually taken in the range  $[0.001; 1]$ . Since the entropy residual  $R_{\text{ent}}(\vec{r}, t)$   
 109 may be extremely large in shocks, the definition of the viscosity coefficients  
 110 also includes a first-order viscosity coefficient that serves as an upper bound for  
 111 the entropy-based viscosity coefficients. The first-order viscosity coefficients,  
 112 denoted by  $\mu_{\text{max}}$  and  $\kappa_{\text{max}}$ , are chosen so that the numerical scheme becomes  
 113 equivalent to an upwind scheme when the first-order coefficients are employed.  
 114 The upwind scheme is known to be over-dissipative but guarantees monotonic-  
 115 ity [18]. In practice, the viscosity coefficients only saturate to the first-order  
 116 viscosity coefficients in shocks and are much smaller elsewhere, hence avoiding  
 117 the over-dissipation of the upwind method. The first-order viscosity coefficients  
 118  $\mu_{\text{max}}$  and  $\kappa_{\text{max}}$  are equal and set proportional to the largest local eigenvalue  
 119  $\|\vec{u}\| + c$ :

$$\mu_{\text{max}}(\vec{r}, t) = \kappa_{\text{max}}(\vec{r}, t) = \frac{h}{2} (\|\vec{u}(t, \vec{r})\| + c(t, \vec{r})), \quad (4)$$

120 where  $h$  denotes the local grid size (for higher than linear finite element rep-  
 121 resentations,  $h$  is defined as the ratio of the grid size to the polynomial order  
 122 of the test functions used, see Eq. 2.4 in [17]). For simplicity, the first-order  
 123 viscosity coefficients will only be referred to as  $\kappa_{\text{max}}(\vec{r}, t)$ . In practice, these  
 124 quantities are evaluated within a given cell  $K$  at quadrature points:

$$\kappa_{\text{max}}^K(\vec{r}_q, t) = \frac{h_K}{2} (\|\vec{u}(t, \vec{r}_q)\| + c(t, \vec{r}_q)), \quad (5)$$

125 where  $\vec{r}_q$  denotes the position of a quadrature point. As stated earlier, the  
 126 entropy viscosity coefficients, which we denote by  $\kappa_e$  and  $\mu_e$ , are set proportional  
 127 to the entropy production evaluated by computing the local entropy residual  
 128  $R_{\text{ent}}$ . The definitions also include the inter-element jump  $J[s]$  of the entropy flux,

allowing for the detection of discontinuities other than shocks (e.g., contact).  
 $\kappa_e$  and  $\mu_e$  are computed as follows

$$\mu_e^K(\vec{r}_q, t) = h_K^2 \frac{\max(|R_{\text{ent}}^K(\vec{r}_q, t)|, J^K[s](t))}{\|s - \bar{s}\|_\infty} \quad (6a)$$

$$\kappa_e^K(\vec{r}_q, t) = \text{Pr} \mu_e^K(\vec{r}_q, t), \quad (6b)$$

where  $\|\cdot\|_\infty$  and  $\bar{\cdot}$  denote the  $L_\infty$ -norm and the average operator over the entire computational domain, respectively. The definition of the entropy jump  $J[s]$  is spatial discretization-dependent and examples of definitions can be found in [17] for discontinuous Galerkin discretization. For continuous finite element methods (FEM), the jump of a given quantity is defined as the change of its normal derivative ( $\partial_n = \vec{\nabla} \cdot \vec{n}$ ) across the common face separating the two elements, and will be further referred to as the inter-element jump. We take the largest value over all faces  $f$  present on the boundary  $\partial K$  of element  $K$ :

$$J^K[s](t) = \max_{f \in \partial K} \max_{\vec{r}_q \in f} \left\| \vec{u}(\vec{r}_q, t) \right\| \left\| \vec{\nabla} s(\vec{r}_q, t) \cdot \vec{n}(\vec{r}_q) \right\|_f, \quad (7)$$

where  $\llbracket a(\vec{r}_q) \rrbracket_f$  denotes the inter-element jump in  $a(\vec{r})$  at quadrature point  $\vec{r}_q$  on face  $f$  (the quadrature points  $\vec{r}_q$  are taken on the faces  $f$  of the element  $K$ ). With the definition given in Eq. (7), the jump is constant over each element  $K$  of the computational domain. The denominator  $\|s - \bar{s}\|_\infty$  is used for dimensionality purposes. Currently, there are no theoretical justifications for choosing the denominator beyond a dimensionality argument. Finally, the viscosity coefficients  $\mu$  and  $\kappa$  are as follows:

$$\mu(\vec{r}, t) = \min\left(\mu_e(\vec{r}, t), \mu_{\text{max}}(\vec{r}, t)\right) \quad \text{and} \quad \kappa(\vec{r}, t) = \min\left(\kappa_e(\vec{r}, t), \kappa_{\text{max}}(\vec{r}, t)\right). \quad (8)$$

Given these definitions, we have the following properties. In shock regions, the entropy viscosity coefficients will experience a peak because of entropy production and thus will saturate to the first-order viscosity. The first-order coefficients are known to be over-dissipative and will smooth out any oscillatory behavior. Elsewhere in the domain, entropy production will be small and the viscosity coefficients  $\mu$  and  $\kappa$  will remain small. High-order accuracy for entropy-based viscous stabilization has been demonstrated using several 1-D shock tube examples and various 2-D tests [1, 2, 17].

## 2.2. Issues in the Low-Mach Regime

In the low-Mach Regime, a smooth flow is known to approach the isentropic limit, resulting in very little entropy production. Since the entropy viscosity method is directly based on the evaluation of the local entropy production, it is of interest to study how the entropy viscosity coefficients  $\mu_e$  and  $\kappa_e$  scale in the low-Mach regime. In practice, the entropy residual  $R_{\text{ent}}$  will be very small in that regime and so will be the denominator  $\|s - \bar{s}\|_\infty$ , thus making

the definition of the viscosity coefficients in Eq. (6) undetermined and likely ill-scaled. One possible approach would consist of expanding the numerator and denominator in terms of the Mach number and deriving its limit when the Mach number goes to zero. Such derivation may not be straightforward, especially for general equations of state. However, this can be avoided by noting that the entropy residual  $R_{\text{ent}}$  can be recast as a function of pressure, density, velocity, and speed of sound as will be shown in Eq. (9) of Section 3.1. This alternate entropy residual definition is the basis for the low-Mach analysis carried out in this paper and possesses several advantages that are detailed next.

### 3. An All-speed Reformulation of the Entropy Viscosity Method

In this section, the entropy residual  $R_{\text{ent}}$  is recast as a function of pressure, density, velocity and speed of sound. Then, a low-Mach asymptotic study is carried out for the Euler equations with viscous regularization in order to derive an appropriate normalization parameter that is valid in the isentropic low-Mach regime as well as for transonic and supersonic flows.

#### 3.1. New Definition of the Entropy Production Residual

The first step in defining viscosity coefficients that behave well in the low-Mach limit is to recast the entropy residual in terms of thermodynamic variables. This provides physical insight on possible normalization choices that can be valid in both low-Mach and transonic flows. The alternate definition of the entropy residual, the derivation of which is given in Appendix A, is the following:

$$R_{\text{ent}}(\vec{r}, t) := \partial_t s + \vec{u} \cdot \vec{\nabla} s = \frac{Ds}{Dt} = \frac{s_e}{P_e} \left( \underbrace{\frac{DP}{Dt} - c^2 \frac{D\rho}{Dt}}_{\tilde{R}_{\text{ent}}(\vec{r}, t)} \right), \quad (9)$$

where  $\frac{D}{Dt}$  denotes the material derivative ( $\frac{D}{Dt} := \frac{\partial}{\partial t} + \vec{u} \cdot \vec{\nabla}$ ), and  $x_y$  is the standard shorthand notation for the partial derivative of  $x$  with respect to  $y$ , e.g.,  $P_e := \frac{\partial P}{\partial e}$ . The entropy residuals  $R_{\text{ent}}$  and  $\tilde{R}_{\text{ent}}$  are proportional to one another and will experience similar variations in space and time. Thus, one may elect to employ  $\tilde{R}_{\text{ent}}$  instead of  $R_{\text{ent}}$  for the evaluation of the local entropy residual. The new expression presents several advantages which include:

- An analytical expression of the entropy function  $s$  is no longer needed: the residual  $\tilde{R}_{\text{ent}}$  is evaluated using the local values of pressure, density, velocity and speed of sound. Deriving an entropy function for some complex equations of state may be difficult;
- Suitable normalizations for the residual  $\tilde{R}_{\text{ent}}$  can be devised. Examples include the pressure itself or combinations of the density, the speed of sound and the norm of the velocity, i.e.,  $\rho c^2$ ,  $\rho c \|\vec{u}\|$  or  $\rho \|\vec{u}\|^2$ .

196 Denoting the normalization of  $\tilde{R}_{\text{ent}}$  by  $\text{norm}_P$ , the entropy-based viscosity co-  
 197 efficients  $\mu_e$  and  $\kappa_e$  can be re-defined as follows:

$$\mu_e^K(\vec{r}, t) = h_K^2 \frac{\max \left( |\tilde{R}_{\text{ent}}^K(\vec{r}_q, t)|, \|\vec{u}(\vec{r}_q, t)\| J^K[P](t), \|\vec{u}(\vec{r}_q, t)\|^2 c^2(\vec{r}_q, t) \|J^K[\rho](t)\| \right)}{\text{norm}_P^\mu}, \quad (10a)$$

198 and

$$\kappa_e^K(\vec{r}, t) = h_K^2 \frac{\max \left( |\tilde{R}_{\text{ent}}^K(\vec{r}_q, t)|, \|\vec{u}(\vec{r}_q, t)\| J^K[P](t), \|\vec{u}(\vec{r}_q, t)\|^2 c^2(\vec{r}_q, t) \|J^K[\rho](t)\| \right)}{\text{norm}_P^\kappa}. \quad (10b)$$

199 Note that now the jump operator acts on the variables appearing in  $\tilde{R}_{\text{ent}}$ ,  
 200 namely, pressure and density. The  $\mu$  and  $\kappa$  coefficients are kinematic viscosities  
 201 (units of  $m^2/s$ ); the normalization parameters  $\text{norm}_P$  are thus in units of pres-  
 202 sure, hence the use of the subscript  $P$ . Note also that we are not requiring the  
 203 same normalization for both  $\mu_e$  and  $\kappa_e$  so the entropy viscosity coefficients can  
 204 be different. The low-Mach asymptotic study presented next will determine the  
 205 proper normalization.

### 206 3.2. Asymptotic Study in the Low-Mach Regime

207 The Euler equations with viscous stabilization, Eq. (6), bear some similari-  
 208 ties with the Navier-Stokes equations in the sense that dissipative terms (con-  
 209 taining second-order spatial derivatives) are present in both sets of equations.  
 210 An abundant literature exists regarding the low-Mach asymptotic of the Navier-  
 211 Stokes equations [9, 10, 11, 19]. The asymptotic study presented here is inspired  
 212 by the work of Muller et al. [19] where an asymptotic derivation for the Navier-  
 213 Stokes was presented. We remind the reader that the objective is to determine  
 214 appropriate scaling for the entropy viscosity coefficients so that the dissipative  
 215 terms remain well-scaled for two limit cases: (i) the isentropic low-Mach limit  
 216 where Euler equations degenerate to an incompressible system of equations in  
 217 the low-Mach limit and (ii) the non-isentropic limit with formation of shocks.  
 218 The isentropic limit of the Euler equations with viscous regularization should  
 219 yield incompressible fluid flow solutions in the low-Mach limit, namely, that  
 220 the pressure fluctuations are of the order  $M^2$  and that the velocity satisfies the  
 221 divergence constraint  $\vec{\nabla} \cdot \vec{u}_0 = 0$  [9, 10, 11]. For non-isentropic situations, shocks  
 222 may form for any value of Mach number and the minimum entropy principle  
 223 should still be satisfied so that numerical oscillations, if any, be controlled by  
 224 the entropy viscosity method independently of the value of the Mach number.  
 225 Our objective is to determine the appropriate scaling for  $\text{norm}_P^\kappa$  and  $\text{norm}_P^\mu$  in  
 226 these two limit cases.

The first step in the study of the limit cases (i) and (ii) is to re-write Eq. (2)

in a non-dimensional manner. To do so, the following variables are introduced:

$$\rho^* = \frac{\rho}{\rho_\infty}, \quad u^* = \frac{u}{u_\infty}, \quad P^* = \frac{P}{\rho_\infty c_\infty^2}, \quad E^* = \frac{E}{c_\infty^2},$$

$$x^* = \frac{x}{L_\infty}, \quad t^* = \frac{t}{L_\infty/u_\infty}, \quad \mu^* = \frac{\mu}{\mu_\infty}, \quad \kappa^* = \frac{\kappa}{\kappa_\infty}, \quad (11)$$

where the subscript  $\infty$  denote the far-field or stagnation quantities and the superscript  $*$  stands for the non-dimensional variables. The far-field reference quantities are chosen such that the dimensionless flow quantities are of order 1. The reference Mach number is given by

$$M_\infty = \frac{u_\infty}{c_\infty}, \quad (12)$$

where  $c_\infty$  is a reference value for the speed of sound. Then, the scaled Euler equations with viscous regularization are:

$$\partial_{t^*} \rho^* + \vec{\nabla}^* \cdot (\rho^* \vec{u}^*) = \frac{1}{\text{Pé}_\infty} \vec{\nabla}^* \cdot (\kappa^* \vec{\nabla}^* \rho^*) \quad (13a)$$

$$\partial_{t^*} (\rho^* \vec{u}^*) + \vec{\nabla}^* \cdot (\rho^* \vec{u}^* \otimes \vec{u}^*) + \frac{1}{M_\infty^2} \vec{\nabla}^* P^* = \frac{1}{\text{Re}_\infty} \vec{\nabla}^* \cdot (\rho^* \mu^* \vec{\nabla}^{s,*} \vec{u}^*)$$

$$+ \frac{1}{\text{Pé}_\infty} \vec{\nabla}^* \cdot (\vec{u}^* \otimes \kappa^* \vec{\nabla}^* \rho^*) \quad (13b)$$

$$\partial_{t^*} (\rho^* E^*) + \vec{\nabla}^* \cdot [\vec{u}^* (\rho^* E^* + P^*)] = \frac{1}{\text{Pé}_\infty} \vec{\nabla}^* \cdot (\kappa^* \vec{\nabla}^* (\rho^* e^*))$$

$$+ \frac{M_\infty^2}{\text{Re}_\infty} \vec{\nabla}^* \cdot (\vec{u}^* \rho^* \mu^* \vec{\nabla}^{s,*} \vec{u}^*) + \frac{M_\infty^2}{2\text{Pé}_\infty} \vec{\nabla}^* \cdot (\kappa^* (u^*)^2 \vec{\nabla}^* \rho^*), \quad (13c)$$

where the numerical Reynolds ( $\text{Re}_\infty$ ) and Péclet ( $\text{Pé}_\infty$ ) numbers are defined as:

$$\text{Re}_\infty = \frac{u_\infty L_\infty}{\mu_\infty} \quad \text{and} \quad \text{Pé}_\infty = \frac{u_\infty L_\infty}{\kappa_\infty}. \quad (14)$$

Note that the Prandtl number used in the original version of the entropy viscosity method is simply given by

$$\text{Pr}_\infty = \text{Pé}_\infty / \text{Re}_\infty. \quad (15)$$

The numerical Reynolds and Péclet numbers defined in Eq. (14) are related to the entropy viscosity coefficients  $\mu_\infty$  and  $\kappa_\infty$ . Thus, once a scaling (in powers of  $M_\infty$ ) is obtained for  $\text{Re}_\infty$  and  $\text{Pé}_\infty$ , the corresponding normalization parameters  $\text{norm}_P^\mu$  and  $\text{norm}_P^\kappa$  will automatically be set. For brevity, the superscripts  $*$  are omitted in the remainder of this section.



For simplicity, we use here the ideal gas equation of state; its non-dimensionalized expression is given by

$$P^* = (\gamma - 1) \rho^* \left( E^* - \frac{1}{2} M_\infty^2 (u^*)^2 \right) = (\gamma - 1) \rho^* e^*. \quad (16)$$

In the low-Mach isentropic limit, shocks cannot form and the compressible Euler equations are known to converge to the incompressible equations when the Mach number tends to zero. When adding dissipative terms, as is the case with the entropy viscosity method, the main properties of the low-Mach asymptotic limit must be preserved. We begin by expanding each variable in powers of the Mach number. As an example, the expansion for the pressure is given by:

$$P(\vec{r}, t) = P_0(\vec{r}, t) + P_1(\vec{r}, t) M_\infty + P_2(\vec{r}, t) M_\infty^2 + \dots \quad (17)$$

By studying the resulting momentum equations for various powers of  $M_\infty$ , it is observed that the leading order and first-order pressure terms,  $P_0$  and  $P_1$ , are spatially constant if and only if  $\text{Re}_\infty = \text{Pe}_\infty = 1$ . In this case, we have at order  $M_\infty^{-2}$ :

$$\vec{\nabla} P_0 = 0 \quad (18a)$$

and at order  $M_\infty^{-1}$

$$\vec{\nabla} P_1 = 0. \quad (18b)$$

Using the scaling  $\text{Re}_\infty = \text{Pe}_\infty = 1$ , the leading-order expressions for the continuity, momentum, and energy equations are:

$$\partial_t \rho_0 + \vec{\nabla} \cdot (\rho \vec{u})_0 = \vec{\nabla} \cdot (\kappa \vec{\nabla} \rho)_0 \quad (19a)$$

$$\partial_t (\rho \vec{u})_0 + \vec{\nabla} \cdot (\rho \vec{u} \otimes \vec{u})_0 + \vec{\nabla} P_2 = \vec{\nabla} \cdot (\rho \mu \vec{\nabla}^s \vec{u} + \kappa \vec{u} \otimes \vec{\nabla} \rho)_0 \quad (19b)$$

$$\partial_t (\rho E)_0 + \vec{\nabla} \cdot [\vec{u} (\rho E + P)]_0 = \vec{\nabla} \cdot (\kappa \vec{\nabla} (\rho e))_0 \quad (19c)$$

where the notation  $(fg)_0$  means that we only keep the 0<sup>th</sup>-order terms in the product  $fg$ . The leading-order of the equation of state is given by

$$P_0 = (\gamma - 1) (\rho E)_0. \quad (20)$$

Using Eq. (20), the energy equation can be recast as a function of the leading-order pressure,  $P_0$ , as follows:

$$\partial_t P_0 + \gamma \vec{\nabla} \cdot (\vec{u} P)_0 = \vec{\nabla} \cdot (\kappa \vec{\nabla} (P))_0. \quad (21)$$

From Eq. (18a), we infer that  $P_0$  is spatially constant. Thus, Eq. (21) becomes

$$\frac{1}{\gamma P_0} \frac{dP_0}{dt} = -\vec{\nabla} \cdot \vec{u}_0 \quad (22)$$

and, at steady state, we have

$$\vec{\nabla} \cdot \vec{u}_0 = 0. \quad (23)$$

264 That is, the leading-order of velocity is divergence-free. The same reasoning can  
 265 be applied to the leading-order of the continuity equation (Eq. (19a)) to show  
 266 that the material derivative of the density variable is zero:

$$\frac{D\rho_0}{Dt} := \partial_t \rho_0 + \vec{u}_0 \cdot \vec{\nabla} \cdot \rho_0 = 0. \quad (24)$$

267 Therefore, we conclude that by setting the Reynolds and Péclet numbers to  
 268 one, the incompressible fluid results are retrieved in the low-Mach limit when  
 269 employing the compressible Euler equations with viscous regularization terms  
 270 present. In addition, the scaling of the Prandtl number can also be obtained  
 271 using Eq. (15), hence clarifying the use of the numerical Prandtl in the original  
 272 entropy viscosity method [1].

### 273 3.3. *Scaling of $Re_\infty$ and $Pé_\infty$ for non-isentropic flows*

274 Next, we consider the non-isentropic case. Recall that even subsonic flows  
 275 can present shocks (for instance, a step initial condition in the pressure will trig-  
 276 ger shock formation, independently of the Mach number). The non-dimensional  
 277 form of the Euler equations given in Eq. (13) provides some insight on the dom-  
 278 inant terms as a function of the Mach number. This is particular obvious in  
 279 the momentum equation, Eq. (13b), where the gradient of pressure is scaled by  
 280  $1/M_\infty^2$ . In the non-isentropic case, we no longer have  $\frac{\vec{\nabla} P}{M_\infty^2} = \vec{\nabla} P_2$  and there-  
 281 fore the pressure gradient term may need to be stabilized by some dissipative  
 282 terms of the same scaling so as to prevent spurious oscillations from forming.  
 283 By inspecting the dissipative terms presents in the the momentum equation,  
 284 having a dissipative term that scales as  $1/M_\infty^2$  leads to the following three op-  
 285 tions: (a)  $Re_\infty = M_\infty^2$  and  $Pé_\infty = 1$ , (b)  $Re_\infty = 1$  and  $Pé_\infty = M_\infty^2$ , or (c)  
 286  $Re_\infty = Pé_\infty = M_\infty^2$ . Any of these choices will also affect the stabilization of  
 287 the continuity and energy equations. For instance, using a Péclet number equal  
 288 to  $M_\infty^2$  may effectively stabilize the continuity equation in the shock region but  
 289 this may also add an excessive amount of dissipation for subsonic flows at the  
 290 location of the contact wave. Such a behavior may not be suitable for accuracy  
 291 purpose, making options (b) and (c) inappropriate. The same reasoning, left to  
 292 the reader, can be carried out for the energy equation (Eq. (13c)) and results in  
 293 the same conclusion. The remaining choice, option (a), has the proper scaling:  
 294 in this case, only the dissipation terms involving  $\vec{\nabla}^{s,*} \vec{u}^*$  scale as  $1/M_\infty^2$  since  
 295  $Re_\infty = M_\infty^2$ , leaving the regularization of the continuity equation unaffected  
 296 because  $Pé_\infty = 1$ .

### 297 3.4. *An All-speed normalization of the entropy residual*

298 The study of the above limit cases yields two different possible scalings for  
 299 the Reynolds number:  $Re_\infty = 1$  in the low-Mach limit and  $Re_\infty = M_\infty^2$  for  
 300 non-isentropic flows, whereas the numerical Péclet number always scales as one.  
 301 In order to have a stabilization method valid for a wide range of Mach numbers,  
 302 from very low-Mach to supersonic flows, these two scalings should be combined  
 303 in a unique definition.

304 We begin with the normalization parameter  $\text{norm}_P^\kappa$ . Using the definition of  
 305 the viscosity coefficients given in Eq. (10) and the scaling of Eq. (11), it can be  
 306 shown that:

$$\kappa_\infty = \frac{\rho_\infty c_\infty^2 u_\infty L}{\text{norm}_{P,\infty}^\kappa}, \quad (25)$$

307 where  $\text{norm}_{P,\infty}$  is the reference far-field quantity for the normalization paramete-  
 308 rer  $\text{norm}_P$ . Substituting Eq. (25) into Eq. (14) and recalling that the numerical  
 309 Péclet number scales as unity, we obtain:

$$\text{norm}_{P,\infty}^\kappa = \text{Pé}_\infty \rho_\infty c_\infty^2 = \rho_\infty c_\infty^2. \quad (26)$$

310 Eq. (26) provides a proper normalization factor to define the  $\kappa$  viscosity coeffi-  
 311 cient. The derivation for  $\text{norm}_P^\mu$  is similar and yields

$$\text{norm}_P^\mu = \text{Re}_\infty \rho_\infty c_\infty^2 = \begin{cases} \rho \|\vec{u}\|^2 & \text{for non-isentropic flows} \\ \rho c^2 = \text{norm}_P^\kappa & \text{for low-Mach flows} \end{cases}. \quad (27)$$

312 A smooth function to transition between these two states is as follows:

$$\sigma(M) = \frac{\tanh(a(M - M^{\text{thresh}})) + |\tanh(a(M - M^{\text{thresh}}))|}{2}, \quad (28)$$

313 where  $M^{\text{thresh}}$  is a threshold Mach number value beyond which the flow is no  
 314 longer considered to be low-Mach (we use  $M^{\text{thresh}} = 0.05$ ),  $M$  is the local  
 315 Mach number, and the scalar  $a$  determines how rapidly the transition from  
 316  $\text{norm}_P^\mu = \rho c^2$  to  $\text{norm}_P^\mu = \rho \|\vec{u}\|^2$  occurs in the vicinity of  $M^{\text{thresh}}$  (we use  
 317  $a = 3$ ). It is easy to verify that

$$\text{norm}_P^\mu = (1 - \sigma(M))\rho c^2 + \sigma(M)\rho \|\vec{u}\|^2 \quad (29)$$

318 satisfies Eq. (27). Finally, we summarize the definition of the viscosity coeffi-  
 319 cients  $\mu$  and  $\kappa$  for completeness:

$$\kappa(\vec{r}, t) = \min(\mu_{\text{max}}(\vec{r}, t), \kappa_e(\vec{r}, t)), \quad (30a)$$

320

$$\mu(\vec{r}, t) = \min(\mu_{\text{max}}(\vec{r}, t), \mu_e(\vec{r}, t)), \quad (30b)$$

321 where the first-order viscosity is given by

$$\kappa_{\text{max}}(\vec{r}, t) = \mu_{\text{max}}(\vec{r}, t) = \frac{h}{2}(\|\vec{u}\| + c) \quad (30c)$$

322 and the entropy viscosity coefficients by

$$\kappa_e(\vec{r}, t) = \frac{h^2 \max(\tilde{R}_{\text{ent}}, J)}{\rho c^2} \text{ and } \mu_e(\vec{r}, t) = \frac{h^2 \max(\tilde{R}_{\text{ent}}, J)}{\text{norm}_P^\mu} \quad (30d)$$

323 with the jumps given by

$$J = \max(\|\vec{u}\| |[\vec{\nabla} P \cdot \vec{n}]|, \|\vec{u}\| c^2 |[\vec{\nabla} \rho \cdot \vec{n}]|) \quad (30e)$$

where  $\text{norm}_P^\kappa$  is computed from Eq. (29). The jump  $J$  is a function of the jump of pressure and density gradients across the face with respect to its normal vector  $\vec{n}$ . Then, the largest value over all faces is determined and used in the definition of the viscosity coefficients. With the definition of the viscosity coefficients  $\mu$  and  $\kappa$  proposed in Eq. (30), the dissipative terms are expected to scale appropriately for very low-Mach regimes as well for transonic and supersonic flows.

#### 4. Extension of the entropy viscosity technique Euler equations with variable area

Fluid flows in nozzles and in pipes of varying cross-sectional area can be modeled using the variable-area variant of the Euler equations, where the conservative variables are now multiplied by the area  $A$ . In addition, these equations differ from the standard Euler equations in that the momentum equation Eq. (31b) contains a non-conservative term proportional to the area gradient. Here, the variable area is assumed to be a smooth function of space only.

$$\partial_t (\rho A) + \vec{\nabla} \cdot (\rho \vec{u} A) = 0, \quad (31a)$$

$$\partial_t (\rho \vec{u} A) + \vec{\nabla} \cdot [A (\rho \vec{u} \otimes \vec{u} + P \mathbb{I})] = P \vec{\nabla} A, \quad (31b)$$

$$\partial_t (\rho E A) + \vec{\nabla} \cdot [\vec{u} A (\rho E + P)] = 0. \quad (31c)$$

The application of the entropy viscosity method to the Euler equations with variable area is not fundamentally different to its application to the standard Euler equations. However, we need to derive the associated dissipative terms and verify that the entropy minimum principle is still satisfied. The variable-area Euler equations with viscous regularization are given below; details of the derivation are provided in Appendix B.

$$\partial_t (\rho A) + \vec{\nabla} \cdot (\rho \vec{u} A) = \vec{\nabla} \cdot (A \kappa \vec{\nabla} \rho), \quad (32a)$$

$$\partial_t (\rho \vec{u} A) + \vec{\nabla} \cdot [A (\rho \vec{u} \otimes \vec{u} + P \mathbb{I})] = P \vec{\nabla} A + \vec{\nabla} \cdot \left[ A \left( \mu \rho \vec{\nabla}^s \vec{u} + \kappa \vec{u} \otimes \vec{\nabla} \rho \right) \right], \quad (32b)$$

$$\partial_t (\rho A E) + \vec{\nabla} \cdot [\vec{u} A (\rho E + P)] = \vec{\nabla} \cdot \left[ A \left( \kappa \vec{\nabla} (\rho e) + \frac{1}{2} \|\vec{u}\|^2 \kappa \vec{\nabla} \rho + \rho \mu \vec{u} \vec{\nabla}^s \vec{u} \right) \right]. \quad (32c)$$

The dissipative terms are quite similar to the ones obtained for the standard Euler equations: each dissipative flux is simply multiplied by the variable area  $A$  in order to ensure conservation of the dissipative flux. When assuming a constant area, Eqs. 2 are recovered.

A low-Mach asymptotic limit of the Euler equations with variable area on the same model as in Section 3.2 will lead to the divergence constraint  $\vec{\nabla} \cdot (\vec{u} A) = 0$  that can be recast as  $\vec{\nabla} \cdot \vec{u} = -\vec{u} \cdot \vec{\nabla} A / A$ . The gradient of the area acts as a source term and will force the fluid to accelerate or decelerate, depending on its sign.

## 357 5. Discretizations and Solution Techniques

358 In this section, we briefly describe the spatial and temporal discretizations  
 359 and the solution techniques used to solve the system of equations Eq. (32). For  
 360 conciseness, we re-write the system of equations in the following form:

$$\partial_t \mathbf{U} + \vec{\nabla} \cdot \vec{\mathbf{F}}(\mathbf{U}) = \mathbf{S} + \vec{\nabla} \cdot \mathbf{D}(\mathbf{U}) \vec{\nabla} \mathbf{U} \quad (33)$$

361 where  $\mathbf{U} = [\rho A, \rho \vec{u} A, \rho E A]^T$  is the solution vector,  $\mathbf{F}$  denotes the inviscid flux

$$\vec{\mathbf{F}} \equiv \begin{bmatrix} \rho u A \\ (\rho u^2 + p) A \\ u(\rho E + P) A \end{bmatrix} \quad (34)$$

362 and  $\mathbf{S}$  is a source term that contains the non-conservative term  $P \vec{\nabla} A$ . The term  
 363  $\vec{\nabla} \cdot \mathbf{D}(\mathbf{U}) \vec{\nabla} \mathbf{U}$  stands for the artificial dissipative terms.

### 364 5.1. Spatial and Temporal Discretizations

365 The system of equations given in Eq. (33) is discretized using a continuous  
 366 Galerkin finite element method and temporal integrators available through the  
 367 MOOSE multiphysics framework [13].

#### 368 5.1.1. Continuous Finite Elements

In order to apply the continuous finite element method, Eq. (33) is multiplied  
 by a test function  $\mathbf{W}(\vec{r})$ , integrated by parts and each integral is decomposed  
 into a sum of integrals over each element  $K$  of the discrete mesh  $\Omega$ . The following  
 weak form is obtained:

$$\begin{aligned} \sum_K \int_K \partial_t \mathbf{U} \mathbf{W} - \sum_K \int_K \vec{\mathbf{F}}(\mathbf{U}) \cdot \vec{\nabla} \mathbf{W} + \int_{\partial\Omega} \vec{\mathbf{F}}(\mathbf{U}) \cdot \vec{n} \mathbf{W} - \sum_K \int_K \mathbf{S} \mathbf{W} \\ + \sum_K \int_K \mathbf{D}(\mathbf{U}) \vec{\nabla} \mathbf{U} \cdot \vec{\nabla} \mathbf{W} - \int_{\partial\Omega} \mathbf{D}(\mathbf{U}) \vec{\nabla} \mathbf{U} \cdot \vec{n} \mathbf{W} = 0. \end{aligned} \quad (35)$$

369 The integrals over the elements  $K$  are evaluated using a numerical quadrature.  
 370 The MOOSE framework provides a wide range of test functions and quadrature  
 371 rules. Linear Lagrange polynomials are employed as test functions in the re-  
 372 sults section. Second-order spatial convergence will be demonstrated for smooth  
 373 solutions.

#### 374 5.1.2. Temporal integration

375 The MOOSE framework offers both first- and second-order explicit and im-  
 376 plicit temporal integrators. In all of the numerical examples presented in Sec-  
 377 tion 6, the temporal derivative will be evaluated using the second-order, back-  
 378 ward difference temporal integrator BDF2. By considering three consecutive

379 solutions,  $\mathbf{U}^{n-1}$ ,  $\mathbf{U}^n$  and  $\mathbf{U}^{n+1}$ , at times  $t^{n-1}$ ,  $t^n$  and  $t^{n+1}$ , respectively, BDF2  
 380 can be expressed as:

$$\int_K \partial_t \mathbf{U} \mathbf{W} = \int_K (\omega_0 \mathbf{U}^{n+1} + \omega_1 \mathbf{U}^n + \omega_2 \mathbf{U}^{n-1}) \mathbf{W}, \quad (36)$$

with

$$\omega_0 = \frac{2\Delta t^{n+1} + \Delta t^n}{\Delta t^{n+1} (\Delta t^{n+1} + \Delta t^n)}, \quad \omega_1 = -\frac{\Delta t^{n+1} + \Delta t^n}{\Delta t^{n+1} \Delta t^n},$$

$$\text{and } \omega_2 = \frac{\Delta t^{n+1}}{\Delta t^n (\Delta t^{n+1} + \Delta t^n)}$$

381 where  $\Delta t^n = t^n - t^{n-1}$  and  $\Delta t^{n+1} = t^{n+1} - t^n$ .

### 382 5.2. Boundary conditions

383 Boundary conditions are implemented by performing a characteristic decom-  
 384 position to compute the appropriate flux at the boundaries. Our implementation  
 385 of the subsonic boundary conditions is inspired by the method described in [20]  
 386 and was adapted for a time implicit solver. Neumann boundary conditions are  
 387 used for all of the boundary types, except for the inlet supersonic boundary that  
 388 are strongly imposed with Dirichlet boundary conditions.

389 For each numerical solution presented in Section 6, the type of boundary con-  
 390 ditions used will be specified and taken among the following: supersonic inlet,  
 391 subsonic inlet (stagnation pressure boundary), subsonic outlet, and supersonic  
 392 outlet. The artificial diffusion coefficient  $D(\mathbf{U})$  is set to zero at the boundary of  
 393 the computational domain so that the boundary term  $\int_{\partial\Omega} D(\mathbf{U}) \vec{\nabla} \mathbf{U} \cdot \vec{n} \mathbf{W}$  stem-  
 394 ming from the integration by parts of the artificial dissipative terms in Eq. (35)  
 395 is ignored.

### 396 5.3. Solver

397 A Jacobian-free-Newton-Krylov (JFNK) method is used to solve for the so-  
 398 lution at the end of each time step. An approximate Jacobian matrix of the  
 399 discretized equations was derived and implemented. Obtaining the matrix en-  
 400 tries requires that the partial derivatives of pressure with respect to the conser-  
 401 vative variables be known (this is relatively simple for the stiffened and ideal  
 402 gas equations of state but may be more complex for general equations of state).  
 403 The contributions of the artificial dissipative terms to the Jacobian matrix are  
 404 approximated by lagging the viscosity coefficients (computing them with the  
 405 previous solution). For instance, this is shown in Eq. (37) for the dissipative  
 406 terms present in the continuity equation:

$$\frac{\partial}{\partial \mathbf{U}} \left( \kappa \vec{\nabla} \cdot \rho \vec{\nabla} W \right) \simeq \kappa \vec{\nabla} \cdot \frac{\partial \rho}{\partial \mathbf{U}} \vec{\nabla} W, \quad (37)$$

407 where  $\mathbf{U}$  denotes any of the conservative variables and  $W$  denotes the component  
 408 of  $\mathbf{W}$  associated with the continuity equation. In the above, we have neglected  
 409  $\frac{\partial \kappa}{\partial \mathbf{U}}$ .

## 6. Numerical Results

1-D and 2-D numerical solutions for the Euler equations with viscous regularization solved using the entropy viscosity method are presented here. Our results show that the new definitions for the viscosity coefficients are robust in the low-Mach limit as well as for transonic and supersonic flows and that shocks are appropriately resolved.

The first set of 1-D simulations consist of liquid water and steam flowing in a converging-diverging nozzle. This test is of interest for multiple reasons: (a) a steady state can be reached (some stabilization methods are known to have difficulties reaching a steady state, [3, 4]), (b) an analytical solution is available and a space-time convergence study can be performed, (c) it can be performed for liquid and gas phases, wherein the gas phase simulation presents a shock while the liquid-phase simulation has a significantly lower Mach number. Next, a 1-D shock tube test (in a straight pipe), taken from the Leblanc test-case suite [21], is performed. This test is known to be more challenging than Sod shock tubes and the fluid's Mach number varies spatially between 0 and 5. A convergence study is also performed to demonstrate convergence of the numerical solution to the exact solution. A slow moving shock is also investigated [22]. This test helps in assessing the ability of the method to damp the post-shock low frequency noise (oscillations). Finally, a strong shock for a liquid phase (Mach number around 0.1) is also performed [23].

The initial conditions for the aforementioned 1-D test cases are given in Table 1.

$\rho_{\text{left}}$	$u_{\text{left}}$	$P_{\text{left}}$	$\rho_{\text{right}}$	$u_{\text{right}}$	$P_{\text{right}}$
Leblanc shock tube (Section 6.3)					
1	0	$4 \cdot 10^{-2}$	$10^{-3}$	0	$4 \cdot 10^{-11}$
Strong shock for liquid phase (Section 6.4)					
1000	0	$10^9$	1000	0	$10^5$
Slow moving shock (Section 6.5)					
1	-0.81	1	3.86	-3.44	10.33

Table 1: Initial conditions for the 1-D test cases (density in  $kg/m^3$ , velocity in  $m/s$ , pressure in  $Pa$ ).

The 2-D simulations are outlined next. First, 2-D subsonic flows around a cylinder [11] and over a circular hump [24] are presented for various far-field Mach numbers (as low of  $10^{-7}$ ). Numerical results of a supersonic flow over a compression corner are provided to illustrate the ability of the new viscosity definitions to handle supersonic flows. Convergence studies are performed when analytical solutions are available.

For each simulation, data relative to the boundary conditions, the Courant-Friedrichs-Lewy number ( $CFL$ ), mesh and equation of state are provided. All of

the numerical solutions presented are obtained using BDF2 as temporal integrator and linear (1-D mesh),  $\mathbb{P}_1$  (2-D triangular mesh), and  $\mathbb{Q}_1$  (2-D quadrangular mesh) finite elements. The spatial integrals are numerically computed using a second-order Gauss quadrature rule. Steady-state is detected in a transient simulation by monitoring the nonlinear residual before proceeding with the Newton solves for a given time step. The ideal gas [25] or stiffened gas equations of state [26] are used; a generic expression is given in Eq. (38).

$$P = (\gamma - 1)\rho(e - q) - \gamma P_\infty \quad (38)$$

where the parameters  $\gamma$ ,  $q$ , and  $P_\infty$  are fluid-dependent and are given in Table 2. The ideal gas equation of state is recovered by setting  $q = P_\infty = 0$  in Eq. (38). The entropy function for the stiffened gas equation of state is concave and given

Table 2: Stiffened Gas Equation of State parameters for steam and liquid water.

fluid	$\gamma$	$C_v$ ( $J.kg^{-1}.K^{-1}$ )	$P_\infty$ (Pa)	$q$ ( $J.kg^{-1}$ )
liquid water (Section 6.1)	2.35	1816	$10^9$	$-1167 \cdot 10^3$
steam (Section 6.2)	1.43	1040	0	$2030 \cdot 10^3$
liquid water (Section 6.4)	4.4	1000	$6 \cdot 10^8$	0

by

$$s = C_v \ln \left( \frac{P + P_\infty}{\rho^{\gamma-1}} \right),$$

where  $C_v$  is the heat capacity at constant volume.

Finally, the convergence rates are computed using the following relation

$$\text{rate}_h = \ln \left( \frac{\|U_{2h} - U_{\text{exact}}\|}{\|U_h - U_{\text{exact}}\|} \right) / \ln 2 \quad (39)$$

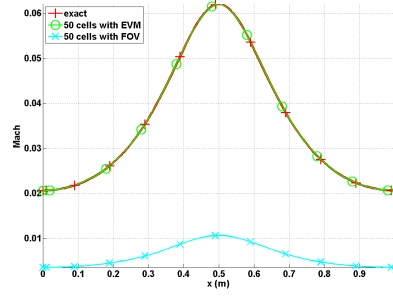
where  $\|\cdot\|$  denotes either the  $L_1$  or  $L_2$  norms and  $h$  is the characteristic grid size.

#### 6.1. Liquid water in a 1-D converging-diverging nozzle

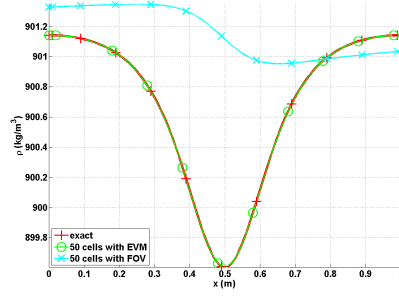
A simulation for liquid flow through a 1-D converging-diverging nozzle is performed. The variable area expression is given by  $A(x) = 1 + 0.5 \cos(2\pi x/L)$  with length  $L = 1m$ . At the inlet, the stagnation pressure and temperature are set to  $P_0 = 1MPa$  and  $T_0 = 453K$ , respectively. At the outlet, only the static pressure is specified:  $P_s = 0.5MPa$ . Initially, the liquid is at rest, the temperature is uniform and equal to the stagnation temperature and the pressure linearly decreases from the stagnation pressure inlet value to the static pressure outlet value. The stiffened gas equation of state is used to model the liquid water with the parameters provided in Table 2. Because of the low pressure difference between the inlet and the outlet, the smooth initial conditions, and



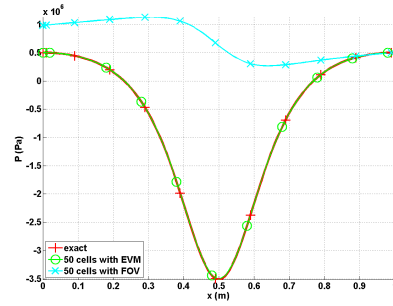
464 the large value of  $P_\infty$  in Eq. (38), the flow remains subsonic and thus displays  
465 no shock. A detailed derivation of the exact steady-state solution can be found  
466 in [27]. A uniform mesh of 50 cells was used to obtain the numerical solution  
467 and the time step size was computed using a *CFL* number of 750. Plots of  
468 the Mach number, density, and pressure are given at steady state in Fig. 1 for  
469 the numerical and exact solutions. The viscosity coefficients are also graphed  
470 in Fig. 1d.



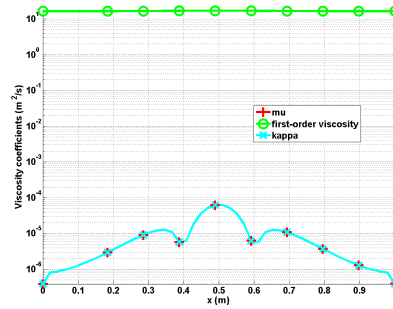
(a) Mach number



(b) Density



(c) Pressure



(d) Viscosity coefficients

Figure 1: Steady-state solution for a fluid flowing through a 1-D converging-diverging nozzle.

471 In Fig. 1, the numerical solutions obtained using the first-order viscosity  
 472 (FOV) and the entropy viscosity method (EVM) are plotted against the ex-  
 473 act solution. The numerical solution obtained with the EVM and the exact  
 474 solution overlap, even for a fairly coarse mesh (50 cells). On the other hand,  
 475 the numerical solution obtained with the FOV does not give the correct steady  
 476 state: this is an illustration of the effect of ill-scaled dissipative terms. Note  
 477 that the entropy viscosity coefficient is very small compared to the first-order  
 478 one (Fig. 1d): (i) the numerical solution is smooth as shown in Fig. 1 and (ii)  
 479 the flow is in a isentropic low-Mach regime A convergence study was performed  
 480 using the exact solution as a reference: the  $L_1$  and  $L_2$  norms of the error and  
 481 the corresponding convergence rates are computed at steady state on various  
 482 uniform meshes from 4 to 256 cells. Spatial convergence results using linear  
 483 finite elements are reported in Table 3 and Table 4 for the primitive variables:  
 484 density, velocity and pressure.

Table 3:  $L_1$  norm of the error for the liquid phase in a 1-D converging-diverging nozzle at steady state.

cells	density	rate	pressure	rate	velocity	rate
4	$2.8037 \cdot 10^{-1}$	—	$8.4705 \cdot 10^5$	—	7.2737	—
8	$1.3343 \cdot 10^{-1}$	1.07	$4.7893 \cdot 10^5$	0.82	6.1493	0.24
16	$2.9373 \cdot 10^{-2}$	2.18	$1.0613 \cdot 10^5$	2.17	1.2275	2.32
32	$5.1120 \cdot 10^{-3}$	2.52	$1.8446 \cdot 10^4$	2.52	$1.8943 \cdot 10^{-1}$	2.69
64	$1.0558 \cdot 10^{-3}$	2.28	$3.7938 \cdot 10^3$	2.28	$3.7919 \cdot 10^{-2}$	2.32
128	$2.3712 \cdot 10^{-4}$	2.15	$8.4471 \cdot 10^2$	2.17	$8.5517 \cdot 10^{-3}$	2.15
256	$5.6058 \cdot 10^{-5}$	2.08	$1.9839 \cdot 10^2$	2.09	$2.0475 \cdot 10^{-3}$	2.06
512	$1.3278 \cdot 10^{-5}$	2.08	$4.6622 \cdot 10^1$	2.09	$4.9516 \cdot 10^{-4}$	2.04
1024	$3.1193 \cdot 10^{-6}$	2.08	$1.1755 \cdot 10^1$	1.99	$1.2379 \cdot 10^{-4}$	2.00

Table 4:  $L_2$  norm of the error for the liquid phase in a 1-D converging-diverging nozzle at steady state.

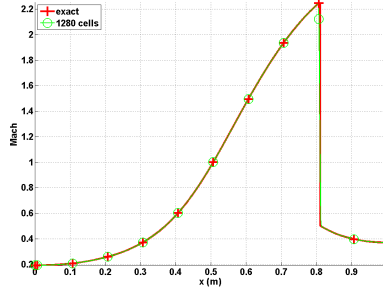
cells	density	rate	pressure	rate	velocity	rate
4	$3.106397 \cdot 10^{-1}$	—	$5.254445 \cdot 10^5$	—	3.288543	—
8	$7.491623 \cdot 10^{-2}$	2.05	$1.636966 \cdot 10^5$	1.68	1.823880	0.85
16	$2.079858 \cdot 10^{-2}$	1.85	$4.627338 \cdot 10^4$	1.49	$4.990605 \cdot 10^{-1}$	0.87
32	$5.329627 \cdot 10^{-3}$	1.96	$1.180287 \cdot 10^4$	1.97	$1.261018 \cdot 10^{-1}$	1.98
64	$1.341583 \cdot 10^{-3}$	1.99	$2.967104 \cdot 10^3$	1.99	$3.160914 \cdot 10^{-2}$	1.99
128	$3.359766 \cdot 10^{-4}$	1.99	$7.428087 \cdot 10^2$	1.99	$7.907499 \cdot 10^{-3}$	1.99
256	$8.403859 \cdot 10^{-5}$	1.99	$1.857861 \cdot 10^2$	1.99	$1.977292 \cdot 10^{-3}$	1.99
512	$2.10075 \cdot 10^{-5}$	2.00	$4.7024 \cdot 10^1$	1.98	$4.9516 \cdot 10^{-4}$	1.99

485 We note that the convergence rates measured in both the  $L_1$  and  $L_2$  norm of

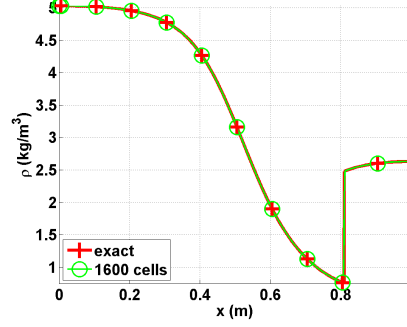
the error are equal to 2; the entropy viscosity method preserves the high-order accuracy of the discretization used when the numerical solution is smooth. The new definition of the entropy viscosity coefficients behaves appropriately in the low-Mach limit.

## 6.2. *Steam in a 1-D converging-diverging nozzle*

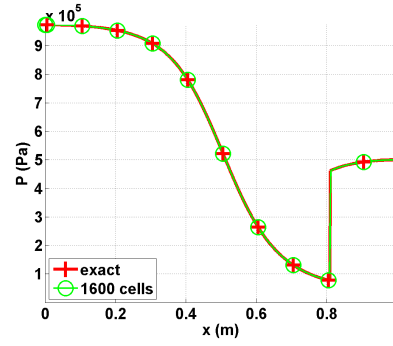
We use the same nozzle geometry, initial conditions and boundary conditions as in the previously example but replace liquid water with steam and use the steam parameters of the stiffened gas equation of state, Table 2. In this example, compressible effects will become dominant. The pressure difference between the inlet and outlet is large enough to accelerate the steam through the nozzle, leading to the formation of a shock in the diverging portion of the nozzle. The behavior is different from the one observed for the liquid water phase in Section 6.1 because of the liquid to gas density ratio is about 1,000. An exact solution at steady state is available for the gas phase [27]. The aim of this section is to show that when using the new definitions of the viscosity coefficients (Eq. (30)), the shock can be correctly resolved without spurious oscillations. The steady-state numerical solution, obtained using a uniform mesh with 1600 cells, is shown in Fig. 2. The  $CFL$  was set to 80 (a high  $CFL$  value can be used because the shock is stationary).



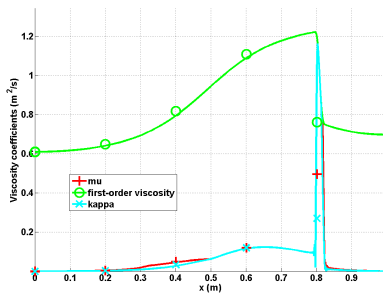
(a) Mach number



(b) Density



(c) Pressure



(d) Viscosity coefficients

21  
Figure 2: Steady-state solution for vapor phase flowing in a 1-D converging-diverging nozzle.

505 The steady-state solution of the density, Mach number and pressure are  
 506 given in Fig. 2. The steady-state solution exhibits a shock around  $x = 0.8m$   
 507 and matches the exact solution. In Fig. 2d, the first-order and entropy viscosity  
 508 coefficients are plotted at steady state (on a log scale): the entropy viscosity  
 509 coefficient is peaked in the shock region around  $x = 0.8m$  where it saturates  
 510 to the first-order viscosity coefficient. The graph also presents another peak at  
 511  $x = 0.5m$  corresponding to the position of the sonic point for the 1-D converging-  
 512 diverging nozzle. This particular point is known to exhibit small instabilities  
 513 that are detected when computing the jumps of the pressure and density gra-  
 514 dients. Elsewhere, the entropy viscosity coefficient is small. In order to prove  
 515 convergence of the numerical solution to the exact solution, a convergence study  
 516 is performed. Because of the presence of a shock, second-order accuracy is not  
 517 expected and the convergence rate of a numerical solution should be 1 and  $1/2$   
 518 when measured in the  $L_1$  and  $L_2$  norms, respectively (see Theorem 9.3 in [28]).  
 519 Results are reported in Table 5 and Table 6 for the primitive variables: density,  
 520 velocity and pressure. The convergence rates for the  $L_1$  and  $L_2$  norms of the er-  
 521 ror computed using Eq. (39) are in good agreement with the theoretical values.

Table 5:  $L_1$  norm of the error for the vapor phase in a 1-D converging-diverging nozzle at steady state.

cells	density	rate	pressure	rate	velocity	rate
5	$0.72562 \cdot 10^{-1}$	—	$1.5657 \cdot 10^5$	—	173.69	—
10	$0.4165 \cdot 10^{-1}$	0.80	$9.6741 \cdot 10^4$	0.63	120.69	0.53
20	$0.20675 \cdot 10^{-1}$	1.01	$4.9193 \cdot 10^4$	0.97	72.149	0.74
40	$0.093703 \cdot 10^{-1}$	1.14	$2.0103 \cdot 10^4$	0.73	34.716	1.06
80	$0.047328 \cdot 10^{-1}$	0.99	$1.0208 \cdot 10^4$	0.98	16.082	1.11
160	$0.023965 \cdot 10^{-2}$	0.98	$5.1969 \cdot 10^3$	0.97	7.9573	1.02
320	$0.020768 \cdot 10^{-2}$	1.03	$2.5116 \cdot 10^3$	1.05	3.7812	1.07
640	$0.0059715 \cdot 10^{-2}$	0.98	$1.2754 \cdot 10^3$	0.98	1.8353	1.04

522

Table 6:  $L_2$  norm of the error for the vapor phase in a 1-D converging-diverging nozzle at steady state.

cells	density	rate	pressure	rate	velocity	rate
5	$9.7144 \cdot 10^{-1}$	—	$2.0215 \cdot 10^5$	—	236.94	—
10	$5.9718 \cdot 10^{-1}$	0.70	$1.3024 \cdot 10^5$	0.63	166.56	0.51
20	$2.9503 \cdot 10^{-1}$	1.02	$6.6503 \cdot 10^4$	0.97	103.36	0.69
40	$1.8193 \cdot 10^{-1}$	0.69	$4.0171 \cdot 10^4$	0.73	66.374	0.64
80	$1.3366 \cdot 10^{-1}$	0.44	$2.3163 \cdot 10^4$	0.44	42.981	0.63
160	$9.6638 \cdot 10^{-2}$	0.47	$1.7263 \cdot 10^4$	0.42	31.717	0.44
320	$7.0896 \cdot 10^{-2}$	0.45	$1.2763 \cdot 10^4$	0.44	23.138	0.45
640	$5.2191 \cdot 10^{-2}$	0.44	$9.4217 \cdot 10^3$	0.44	16.910	0.45

### 6.3. Leblanc shock tube

The 1-D Leblanc shock tube is a Riemann problem designed to test the robustness and the accuracy of stabilization methods. The initial conditions are given in Table 1. The ideal gas equation of state (with  $\gamma = 5/3$ ) is used to compute the pressure. This test is computationally challenging because of the large pressure ratio at the initial interface. The computational domain consists of a 1-D straight pipe of length  $L = 9m$  with the initial interface located at  $x = 2m$ . At  $t = 0s$ , the interface is removed. The numerical solution is run until  $t = 4s$  and the density, momentum and total energy profiles are given in Fig. 3, along with the exact solution. The viscosity coefficients are also plotted in Fig. 3d. These plots were run with three different uniform meshes of 800, 3200, and 6000 cells and a constant  $CFL = 1$ .

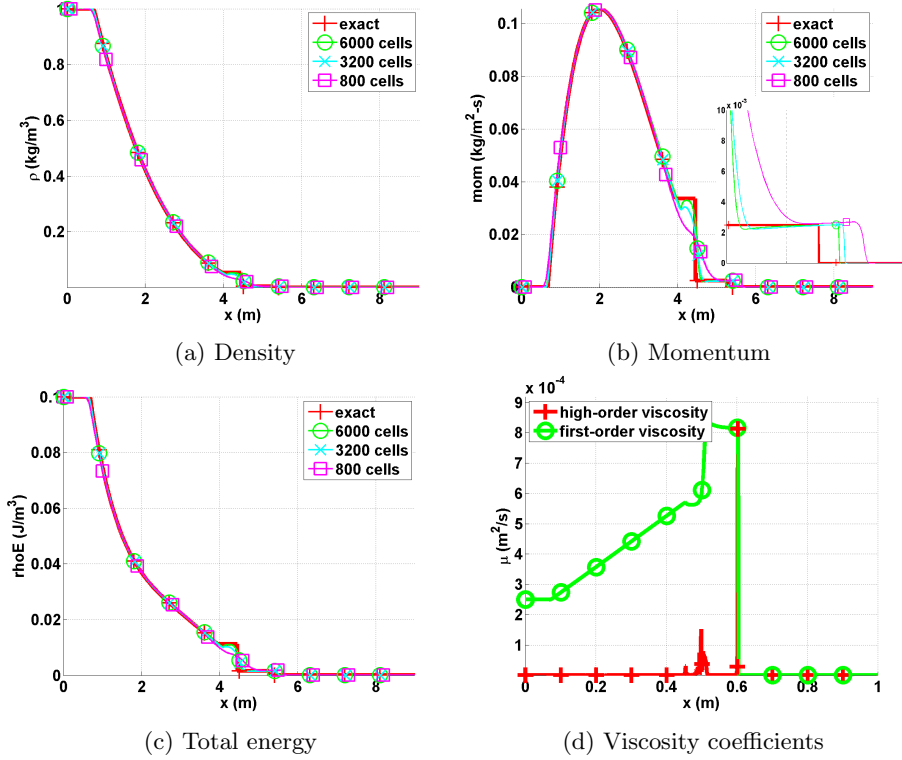


Figure 3: Exact and Numerical solutions for the 1-D Leblanc shock tube at  $t = 4$  s.

The density, momentum and total energy profiles are provided in Fig. 3. In Fig. 3b, the shock region is zoomed in for better resolution: the shock is well resolved. We also observe that the shock position computed numerically converges to the exact position under mesh refinement. The contact wave at  $x = 4.5m$  can be seen in Fig. 3b. The entropy viscosity coefficient profile is shown in Fig. 3d and behaves as expected: it saturates to the first-order viscosity in the shock region, thus preventing oscillations from forming. At the location of the contact wave, a smaller peak is observed and is due to the presence of the jump terms in the definition of the entropy viscosity coefficient (Eq. (30)). The Mach number, not plotted, is of the order of 1.3 just before the shock and reaches a maximum value close to 5 in the contact region.

Once again, a convergence study is performed in order to prove convergence of the numerical solution to the exact solution. As in the previous example (vapor phase in the 1-D nozzle, Section 6.2), the expected convergence rates in the  $L_1$  and  $L_2$  norms are 1 and  $1/2$ , respectively. The exact solution was obtained by running a 1-D Riemann solver and used as the reference solution to compute the  $L_1$  and  $L_2$ -norms that are reported in Table 7 and Table 8 for the



conservative variables: density, momentum and total energy. The convergence rates are again approaching their theoretical values.

Table 7:  $L_1$  norm of the error for the 1-D Leblanc test at  $t = 4s$ .

cells	density	rate	momentum	rate	total energy	rate
100	$1.0354722 \cdot 10^{-2}$	—	$3.5471714 \cdot 10^{-3}$	—	$1.4033046 \cdot 10^{-3}$	—
200	$7.2680512 \cdot 10^{-3}$	0.51	$2.5933119 \cdot 10^{-3}$	0.45	$9.8611746 \cdot 10^{-4}$	0.51
400	$5.0825628 \cdot 10^{-3}$	0.52	$2.0668092 \cdot 10^{-3}$	0.33	$7.7844421 \cdot 10^{-4}$	0.34
800	$3.4025056 \cdot 10^{-3}$	0.58	$1.4793838 \cdot 10^{-3}$	0.48	$5.5702549 \cdot 10^{-4}$	0.48
1600	$2.1649953 \cdot 10^{-3}$	0.65	$9.7152832 \cdot 10^{-4}$	0.61	$3.5720171 \cdot 10^{-4}$	0.64
3200	$1.2465433 \cdot 10^{-3}$	0.79	$5.5937409 \cdot 10^{-4}$	0.79	$2.0491799 \cdot 10^{-4}$	0.80
6400	$6.4476928 \cdot 10^{-4}$	0.95	$3.0244198 \cdot 10^{-4}$	0.89	$1.0914891 \cdot 10^{-4}$	0.91
12800	$3.3950948 \cdot 10^{-4}$	0.93	$1.5958118 \cdot 10^{-4}$	0.92	$5.7909794 \cdot 10^{-5}$	0.91

Table 8:  $L_2$  norm of the error for the 1-D Leblanc test at  $t = 4s$ .

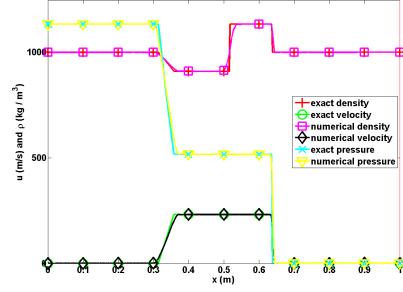
cells	density	rate	momentum	rate	total energy	rate
100	$5.7187851 \cdot 10^{-3}$	—	$1.7767236 \cdot 10^{-3}$	—	$7.6112265 \cdot 10^{-4}$	—
200	$3.8995238 \cdot 10^{-3}$	0.55	$1.4913161 \cdot 10^{-3}$	0.25	$5.5497308 \cdot 10^{-4}$	0.46
400	$2.8103526 \cdot 10^{-3}$	0.47	$1.3305301 \cdot 10^{-3}$	0.16	$4.6063172 \cdot 10^{-4}$	0.27
800	$2.1081933 \cdot 10^{-3}$	0.41	$1.1398931 \cdot 10^{-3}$	0.22	$3.7798953 \cdot 10^{-4}$	0.29
1600	$1.5731052 \cdot 10^{-3}$	0.42	$9.0394227 \cdot 10^{-4}$	0.33	$2.9584646 \cdot 10^{-4}$	0.35
3200	$1.0610667 \cdot 10^{-3}$	0.57	$6.2735595 \cdot 10^{-4}$	0.53	$2.054455 \cdot 10^{-4}$	0.53
6400	$7.3309974 \cdot 10^{-4}$	0.53	$4.4545754 \cdot 10^{-4}$	0.49	$1.4670834 \cdot 10^{-4}$	0.49
12800	$5.1020991 \cdot 10^{-4}$	0.52	$3.1266758 \cdot 10^{-4}$	0.51	$1.0299897 \cdot 10^{-5}$	0.51

#### 6.4. 1-D shock tube with a liquid phase

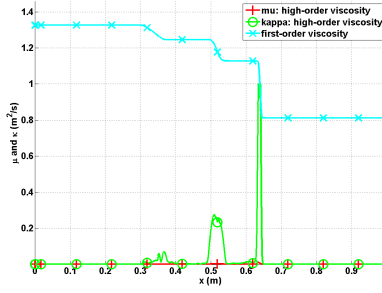
The purpose of this test is to investigate the ability of the entropy viscosity method to stabilize a strong shock with a small Mach number [23] (this reference is for a two-phase flow model but we are only interested in the initial conditions for the liquid phase): the Mach number in the shock region is of the order of 0.1. In this case, as explained in Section 3.2, the viscosity coefficients are required to have different order of magnitude in order to ensure the correct scaling of the dissipative terms. The purpose of this test is to validate the approach presented in Section 3.2.

The stiffened gas equation of state is used to model a liquid flow with the parameters given in Table 2. The computational domain of length  $L = 1m$  is uniformly discretized using 500 cells. The step initial conditions are given in Table 1. The simulation is run with a  $CFL = 1$  until the final time  $t_{\text{final}} = 7 \cdot 10^{-5}s$ . Results for pressure, density, velocity and the viscosity coefficients

are given in Fig. 4 along with the exact solution for comparison purposes. The numerical solution is in good agreement with exact solution in Fig. 4a. The viscosity coefficients  $\mu$  and  $\kappa$  are not equal in the shock because the Mach number is of order 0.1. The viscosity coefficient  $\kappa$  saturates to the first-order viscosity in the shock region around  $x = 0.65m$  and is sufficient to stabilize the numerical scheme.



(a) Density, velocity and pressure profiles.



(b) Viscosity coefficients profile.

Figure 4: Numerical solution for the 1-D liquid shock tube at  $t_{\text{final}} = 7 \cdot 10^{-5} s$ .

#### 6.5. 1-D slow moving shock

Slow moving shocks are known to produce post-shock noise of low frequency that is not damped by some numerical dissipation methods [22]. The aim of this simulation is to test the ability of the entropy viscosity method to dampen the low frequency waves. The 1-D slow moving shock consists of a shock wave moving from left to right with the initial conditions given in Table 1. The ideal gas equation of state is used with a heat capacity ratio  $\gamma = 1.4$ . In order to make the shock travel a significant distance, the final time is taken equal to  $t = 1.1 s$ . A pressure boundary condition is used at the left boundary to let the rarefaction and contact waves exit the domain. The numerical solution, obtained with 200 equally-spaced cells, is given in Fig. 5 and is compared to the exact solution obtained from a Riemann solver. We use a  $CFL$  of 1. With this  $CFL$  value, it takes about 50 time steps for the shock to traverse one cell. The numerical

587 results are in good agreement with the exact solution and do not display any  
 588 post-shock noise. The rarefaction and contact waves are not visible on Fig. 5a  
 589 since they exited the computational domain through the left pressure boundary  
 590 condition earlier. As explained in [29], Godunov's type methods usually fail to  
 591 resolve a slow moving shock because of the nature of the stabilization method:  
 592 the method scales as the eigenvalue of the appropriate field. In the case of a slow  
 593 moving shock, the dissipation added to the system is under-estimated and leads  
 594 to post-shock noise. In the case of the entropy viscosity method, the entropy  
 595 residual detects the shock position and the viscosity coefficients saturate to the  
 596 first-order viscosity values in the shock region. The main difference between a  
 597 Godunov's type method and the entropy viscosity method lies in the definition of  
 598 the first-order viscosity coefficients that are proportional to the *local maximum*  
 599 *eigenvalue*  $||\vec{u}|| + c$  and not to the eigenvalue of the characteristic field.

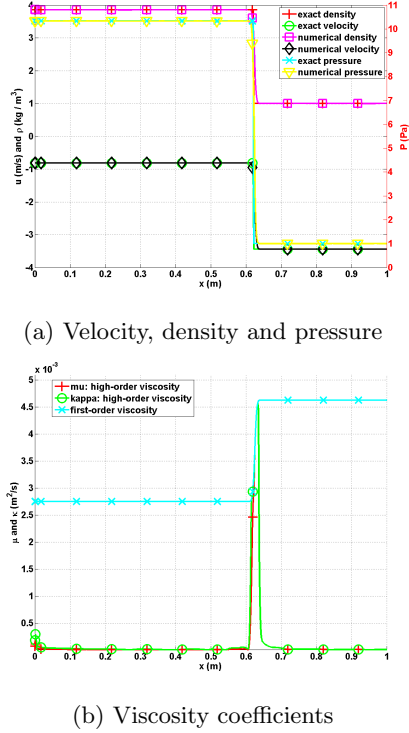


Figure 5: Slow moving shock profiles at  $t = 1.1s$ .

## 6.6. Subsonic flow over a 2-D cylinder

600 Fluid flow over a 2-D cylinder is often used as a benchmark case to test  
 601 numerical schemes in the low-Mach regime [9, 10, 11]. For this test, an analytical  
 602 solution is available in the incompressible limit and is often referred to as the  
 603 potential flow solution. The main features of the potential flow are the following:  
 604

- 605 • The solution is symmetric: the iso-Mach contour lines are used to assess  
606 the symmetry of the numerical solution;
- 607 • The velocity at the top of the cylinder is twice the incoming velocity set  
608 at the inlet;
- 609 • The pressure fluctuations are proportional to the square of inlet Mach  
610 number, i.e.,

$$\delta P = \frac{\max(P(\vec{r})) - \min(P(\vec{r}))}{\max(P(\vec{r}))} \propto M_\infty^2 \quad (40)$$

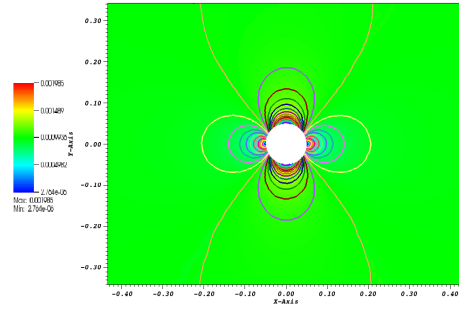
611 where  $\delta P$  and  $M_\infty$  denote the pressure fluctuations and the inlet Mach  
612 number, respectively.

613 The computational domain consists of a  $1 \times 1$  square with a circular hole of  
614 radius 0.05 in its center. A  $\mathbb{P}_1$  triangular mesh with 4008 triangular elements  
615 is employed to discretize the geometry. The ideal gas equation of state, with  
616  $\gamma = 1.4$  is used. At the inlet, a subsonic stagnation boundary condition is  
617 used: the stagnation pressure and temperature are computed using the following  
618 relations:

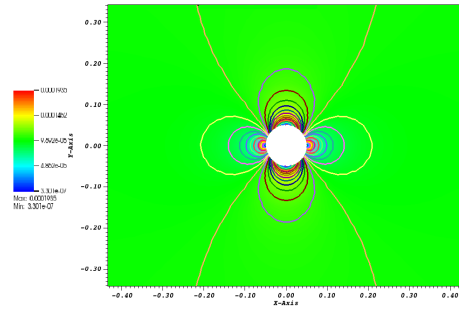
$$\begin{cases} P_0 = P \left(1 + \frac{\gamma-1}{2} M^2\right)^{\frac{\gamma}{\gamma-1}} \\ T_0 = T \left(1 + \frac{\gamma-1}{2} M^2\right) \end{cases} \quad (41)$$

619 A static pressure boundary condition, with static pressure  $P_s = 101,325 \text{ Pa}$ ,  
620 is set at the outlet boundary. The implementation of the pressure boundary  
621 conditions is based on [20]. A solid wall boundary condition is set for the top  
622 and bottom walls of the computational domain. The simulations are run until  
623 a steady state is reached (with a  $CFL$  of 40). When the residual norm (for all  
624 equations) is less than  $10^{-12}$  the steady state is considered to have been reached.

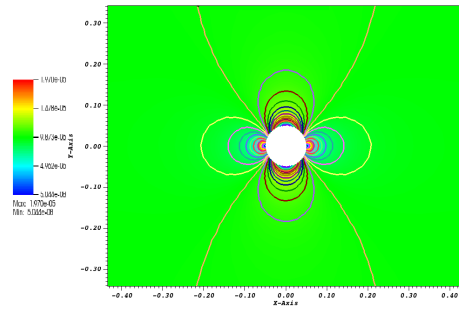
625 Several simulations are performed, with inlet Mach numbers  $M_{\text{inlet}}$  ranging  
626 from  $10^{-3}$  to  $10^{-7}$ , and are shown in Fig. 6. The iso-Mach contour lines are  
627 drawn using 30 equally-spaced intervals, from  $2 \times 10^{-10}$  to  $M_{\text{inlet}}$ .



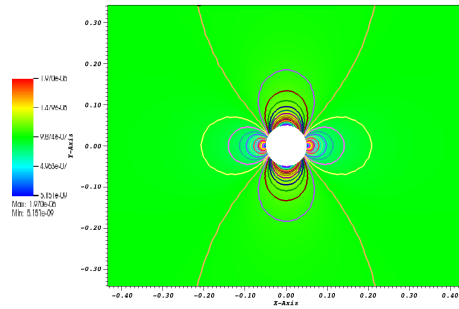
(a)  $M_{\text{inlet}} = 10^{-3}$



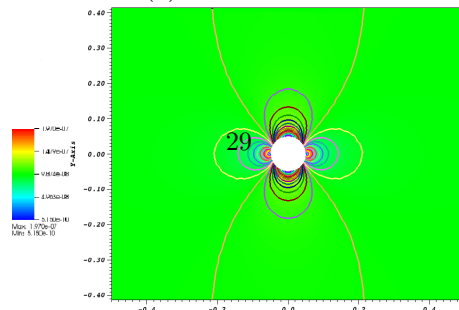
(b)  $M_{\text{inlet}} = 10^{-4}$



(c)  $M_{\text{inlet}} = 10^{-5}$



(d)  $M_{\text{inlet}} = 10^{-6}$



(e)  $M_{\text{inlet}} = 10^{-7}$

628 The velocity at the top of the cylinder and at the inlet are given for different  
629 Mach-number values (ranging from  $10^{-3}$  to  $10^{-7}$ ) in Table 9. The ratio of the  
630 inlet velocity to the velocity at the top of cylinder is also computed and is very  
631 close to the theoretical value of 2 that is expected in the incompressible limit.

Table 9: Velocity ratio for different Mach numbers.

Mach number	inlet velocity	velocity at the top of the cylinder	ratio
$10^{-3}$	$2.348 \cdot 10^{-3}$	$1.176 \cdot 10^{-3}$	1.99
$10^{-4}$	$2.285 \cdot 10^{-4}$	$1.145 \cdot 10^{-4}$	1.99
$10^{-5}$	$2.283 \cdot 10^{-5}$	$1.144 \cdot 10^{-5}$	1.99
$10^{-6}$	$2.283 \cdot 10^{-6}$	$1.144 \cdot 10^{-6}$	1.99
$10^{-7}$	$2.283 \cdot 10^{-7}$	$1.144 \cdot 10^{-7}$	1.99

632 In Fig. 7, the fluctuations in pressure and velocity are plotted as a function  
633 of the Mach number (on a log-log scale). The pressure fluctuations are expected  
634 to be of the order of  $M^2$  in the incompressible limit, which we observe. From  
635 Bernoulli's principle, this implies that the velocity fluctuations should be of  
636 order  $M$  in the incompressible limit, which we also observe in Fig. 7. It is  
637 known that some stabilization methods, e.g., [9, 10, 11], can produce pressure  
638 fluctuations with the wrong Mach-number order. Here, the entropy viscosity  
639 method yields the correct orders in the low-Mach limit. For ease of comparison,  
640 reference lines with slope values of 1 and 2 are also plotted.

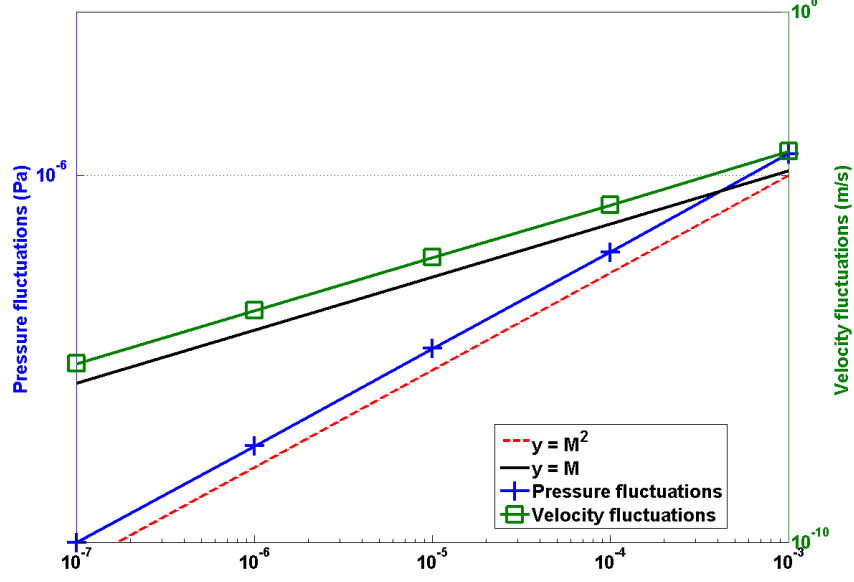


Figure 7: Log-log plot of the pressure and velocity fluctuations as a function of the far-field Mach number.

#### 6.7. Subsonic flow over a 2-D hump

This is another example of an internal flow configuration. It consists of a channel of height  $L = 1\text{ m}$  and length  $3L$ , with a circular bump of length  $L$  and thickness  $0.1L$ . The bump is located on the bottom wall at a distance  $L$  from the inlet. The system is initialized with a uniform pressure  $P = 101,325\text{ Pa}$  and temperature  $T = 300\text{ K}$ . The initial velocity is computed from the inlet Mach number, the pressure, the temperature and the ideal gas equation (with  $\gamma = 1.4$ ). Here,  $C_v = 717\text{ J/kg} \cdot \text{K}$ . At the inlet, a subsonic stagnation boundary condition is used and the stagnation pressure and temperature are computed using Eq. (41). The static pressure  $P_s = 101,325\text{ Pa}$  is set at the subsonic outlet. The results are shown in Fig. 8a, Fig. 8b, Fig. 8c and Fig. 8d for the inlet Mach numbers  $M_\infty = 0.7$ ,  $M_\infty = 0.01$ ,  $M_\infty = 10^{-4}$  and  $M_\infty = 10^{-7}$ , respectively. It is expected that, for low Mach numbers, the solution does not depend on the Mach number and is identical to the incompressible flow solution. On the other hand, for a flow with  $M = 0.7$ , the compressible effects become non negligible and a shock can form. A uniform grid of 3352  $Q_1$  elements was used to obtain the numerical solution for Mach numbers less than and equal to  $M_\infty = 0.01$ . A spatial mesh, once refined, was employed for the  $M_\infty = 0.7$  simulation in order to better resolve the shock. A  $CFL$  of 20 was employed and the simulations were run until steady state.

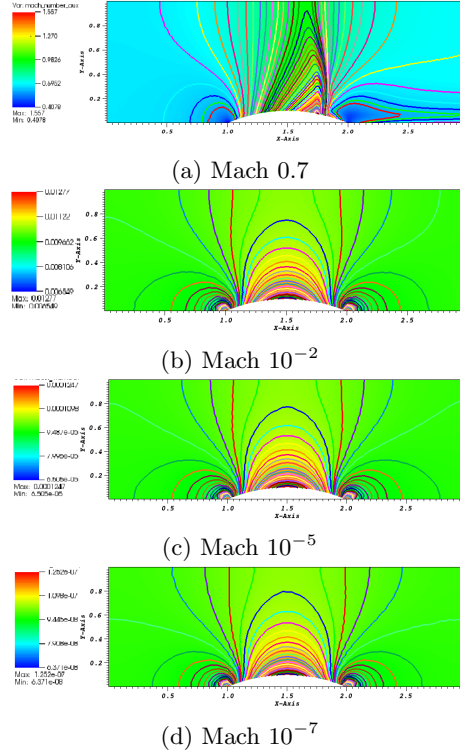


Figure 8: Iso-Mach lines for a 2-D flow over a circular bump (steady-state solution).

The results shown in Fig. 8b, Fig. 8c and Fig. 8d correspond to the low-Mach regime. The iso-Mach lines are drawn ranging from the minimum and the maximum values (provided in each legend) using 50 equally-spaced intervals. The steady-state solution is symmetric and does not depend on the value of the inlet Mach number, as expected in the incompressible limit.

In Fig. 8a, the steady-state numerical solution develops a shock: the compressibility effects are no longer small. The iso-Mach lines are also plotted with 50 intervals and range from 0.4 to 1.6. The shock is well resolved and does not display any instabilities or spurious oscillations.

### 6.8. Supersonic flow in a compression corner

In this last example, we consider a supersonic flow at Mach 2.5 impinging on a corner with an angle of  $15^\circ$ . From the oblique shock theory [15], an analytical solution for this supersonic flow is available and gives the downstream-to-upstream pressure, entropy and Mach number ratios. The initial conditions are chosen to be spatially uniform: the pressure and temperature are set to  $P = 101,325 \text{ Pa}$  and  $T = 300 \text{ K}$ , respectively. The ideal gas equation of state is used with the same parameters as in Section 6.7. The initial velocity is computed from



678 the upstream Mach number. The inlet is supersonic and therefore, the pressure,  
679 temperature and velocity are specified using Dirichlet boundary conditions. The  
680 outlet is also supersonic and none of the characteristics enter the domain through  
681 this boundary; the values are computed by the solver.

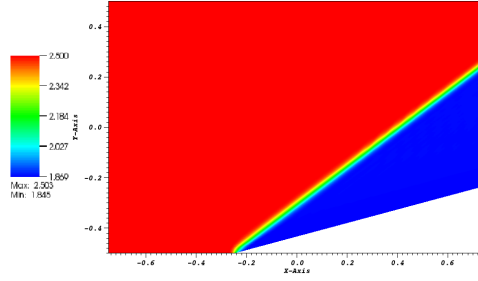
682 The simulation is run with  $CFL = 2$  until steady state is reached. A 2-D  
683 mesh made of 16,109  $\mathbb{Q}_1$  elements is used. The ratios for pressure, entropy and  
684 Mach number computed using the analytical (published with only two significant  
685 digits) and the numerical solutions are given in Table 10; they are in excellent  
686 agreement. The shock wave angle at steady state is also known and given by  
687 the so-called  $\theta - \beta - M$  relation:

$$\tan \theta = 2 \cot \beta \frac{M^2 \sin^2 \beta - 1}{M^2 (\gamma + \cos^2(2\beta)) + 2}, \quad (42)$$

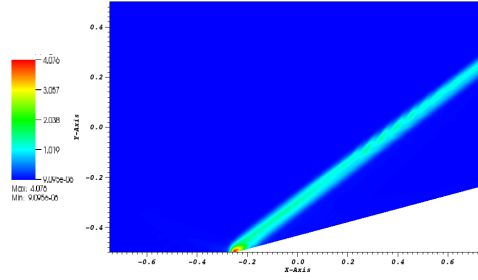
688 where  $\theta$ ,  $\beta$  and  $M$  denote the corner angle, the shock wave angle, and the  
689 upstream Mach number, respectively. For Mach 2.5 and a  $15^\circ$  corner angle, the  
690 analytical value for the shock wave angle is  $36.94^\circ$  at steady state. From Fig. 9a,  
691 the numerical value of the shock wave angle can be measured and is found to  
692 be equal to  $36.9^\circ$  and thus is in excellent agreement with the theory.

	analytical	numerical
Pressure	2.47	2.467
Mach number	0.74	0.741
Entropy	1.03	1.026

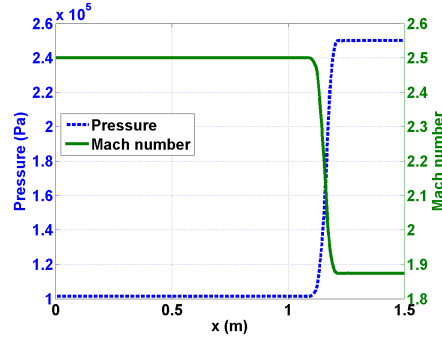
Table 10: Ratio of analytical and numerical downstream to upstream quantities for the compression corner problems (corner angle of  $15^\circ$  and inlet  $M = 2.5$  (analytical values from [15])).



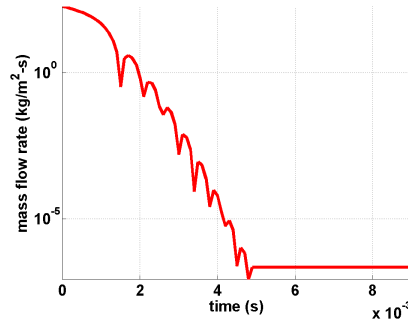
(a) Mach number



(b) Viscosity coefficients



(c) Pressure and Mach number



(d) Difference between inlet and outlet mass flow rates as a function of time.

Figure 9: Steady-state solution for a flow in a 2-D compression corner.

693 The steady-state numerical solution is given in Fig. 9; the Mach number and  
694 the viscosity coefficients are plotted in Fig. 9a and Fig. 9b, respectively. The  
695 steady-state solution is composed of two regions of constant state separated by  
696 an oblique shock. Fig. 9b shows that the viscosity coefficient is large in the shock  
697 and small elsewhere, as expected. At the location of the corner ( $x = -0.25m$ ,  
698  $y = -0.5m$ ), the viscosity coefficient is peaked because of the treatment of the  
699 wall boundary condition: at this particular node, the normal is not well defined  
700 and may cause some numerical errors. The 1-D graphs at  $y = 0$  for the pressure  
701 and the Mach number are given in Fig. 9c: no spurious oscillations are observed  
702 and the shock is well resolved. Finally, the difference between the inlet and  
703 outlet mass flow rates is plotted in Fig. 9d and shows that a steady state has  
704 indeed been reached.

705 The results presented in this paper demonstrate the ability of the entropy  
706 viscosity method with the new definitions of the viscosity coefficients to correctly  
707 simulate several types of flows (from very low Mach subsonic to transonic flows)  
708 without tuning parameters.

## 709 7. Conclusions

710 A new version of the entropy viscosity method that is valid for a wide range  
711 of Mach numbers has been derived and presented for the inviscid Euler equa-  
712 tions. The definition of the viscosity coefficients is now consistent with the  
713 low-Mach asymptotic limit, does not require an analytical expression for the  
714 entropy function, and is therefore applicable to a larger variety of flow regimes,  
715 from very low-Mach flows to supersonic flows. The method has also been ex-  
716 tended to Euler equation with variable area to solve nozzle flow problems. In  
717 1-D, convergence of the numerical solution to the exact solution was demon-  
718 strated by computing the convergence rates of the L1 and L2 norms for flows  
719 in a converging-diverging nozzle and in straight pipes. For smooth solutions,  
720 second-order convergence was verified; solutions with shocks converged with the  
721 expected theoretical rates of 1 (L<sub>1</sub>-norm) and 0.5 (L<sub>2</sub>-norm).

722 The effectiveness of the method was also demonstrated in 2-D using a se-  
723 ries of benchmark problems for both subsonic and supersonic flows in various  
724 geometries, with Mach numbers ranging from  $10^{-7}$  to 2.5. For very low-Mach  
725 flows, we numerically verified that the pressure fluctuations were proportional  
726 to the square of the Mach number, as expected in the incompressible limit.

727 In the future, we plan to further extend the entropy viscosity method to the  
728 seven-equation two-phase flow fluid model [20]. This two-phase flow system of  
729 equations is a good candidate for two reasons: it is unconditionally hyperbolic  
730 and degenerates to the standard Euler equations when one phase disappears.

## 731 Acknowledgments

732 The authors (M.D. and J.R.) would like to thank Bojan Popov and Jean-Luc  
733 Guermond for many fruitful discussions. the research was carried out under the  
734 auspices the Idaho National Laboratory for the US Department of Energy.

## References

- [1] J. L. Guermond, R. Pasquetti, Entropy viscosity method for nonlinear conservation laws, *Journal of Comput. Phys* 230 (2011) 4248–4267.
- [2] J. L. Guermond, R. Pasquetti, Entropy viscosity method for high-order approximations of conservation laws, *Lecture Notes in Computational Science and Engineering* 76 (2011) 411–418.
- [3] B. Cockburn, C. Johnson, C. Shu, E. Tadmor, Advanced numerical approximation of nonlinear hyperbolic equations, *Lecture Notes in Mathematics* 1697.
- [4] B. Cockburn, G. Karniadakis, C. Shu, Discontinuous galerkin methods: theory, computation and applications, *Lecture Notes in Computer Science and Engineering* 11.
- [5] R. Lohner, *Applied CFD Techniques: an Introduction based on Finite Element Methods*, 2<sup>nd</sup> Edition Wiley, 2003.
- [6] A. Lapidus, A detached shock calculation by second order finite differences, *J. Comput. Phys.* 2 (1967) 154–177.
- [7] R. Lohner, K. Morgan, J. Peraire, A simple extension to multidimensional problems of the artificial viscosity due to lapidus, *Commun. Numer. Methods Eng.* 1(14) (1985) 141–147.
- [8] J. Donea, A. Huerta, *Finite Element Methods for Flow Problems*, Oxford University Press, 2003.
- [9] H. Guillard, C. Viozat, On the behavior of upwind schemes in the low mach number limit, *Computers & Fluids* 28 (1999) 63–86.
- [10] E. Turkel, Preconditioned techniques in computational fluid dynamics, *Annu. Rev. Fluid Mech.* 31 (1999) 385–416.
- [11] J. S. W. D. L. Darmofal, J. Peraire, The solution of the compressible euler equations at low mach numbers using a stabilized finite element algorithm, *Comput. Methods Appl. Mech. Engrg.* 190 (2001) 5719–5737.
- [12] X.-S. Li, C.-W. Gu, An all-speed roe-type scheme and its asymptotic analysis of low mach number behavior, *Journal of Computational Physics* 227 (2008) 5144–5159.
- [13] D. Gaston, C. Newsman, G. Hansen, D. Lebrun-Grandie, A parallel computational framework for coupled systems of nonlinear equations, *Nucl. Eng. Design* 239 (2009) 1768–1778.
- [14] J. L. Guermond, B. Popov, Viscous regularization of the euler equations and entropy principles, under review.

- 771 [15] J. D. Anderson, Modern compressible flow, in: Guide for Verification and  
772 Validation in Computational Solid Mechanic., New York, 1982, pp. 10–  
773 2006.
- 774 [16] J. L. Guermond, R. Pasquetti, Entropy-based nonlinear viscosity for four-  
775 rier approximations of conservation laws, in: C.R. Math. Acad. Sci., Vol.  
776 326, Paris, 2008, pp. 801–806.
- 777 [17] V. Zingan, J. L. Guermond, J. Morel, B. Popov, Implementation of the  
778 entropy viscosity method with the discontinuous galerkin method, Journal  
779 of Comput. Phys 253 (2013) 479–490.
- 780 [18] E. F. Toro, Riemann Solvers and numerical methods for fluid dynamics,  
781 2<sup>nd</sup> Edition, Springer, 1999.
- 782 [19] B. Muller, Low-mach number asymptotes of the navier-stokes equations,  
783 Journal of Engineering Mathematics 34 (1998) 97–109.
- 784 [20] R. Berry, R. Saurel, O. LeMetayer, The discrete equation method (dem)  
785 for fully compressible, two-phase flows in ducts of spatially varying cross-  
786 section, Nuclear Engineering and Design 240 (2010) 3797–3818.
- 787 [21] R. Loubere, Validation test case suite for compressible hydrodynamics com-  
788 putation, Theoretical Division T-7 Los Alamos National Laboratory.
- 789 [22] J. J. Quirk, A contribution to the great riemann solver debate, NASA  
790 Contractor Report 191409 ICASE Report No. (1992) 92–64.
- 791 [23] R. Abgrall, R. Saurel, Discrete equations for physical and numerical  
792 compressible multiphase mixtures, Journal of Computational Physics 186  
793 (2003) 361–396.
- 794 [24] D. L. Darmofal, K. Siu, A robust multigrid algorithm for the euler equations  
795 with local preconditioning and semi-coarsening, Journal of Computational  
796 Physics 151 (1999) 728–756.
- 797 [25] P. Perrot, A to Z of Thermodynamics, Oxford University Press, 1998.
- 798 [26] O. LeMetayer, J. Massoni, R. Saurel, Elaborating equation of state for a  
799 liquid and its vapor for two-phase flow models, International Journal of  
800 Thermal Science 43 (2004) 265–276.
- 801 [27] S. LeMartelot, B. Nkonga, R. Saurel, Liquid and liquid-gas flows at all  
802 speeds., Journal of Computational Physics 255 (2013) 53–82.
- 803 [28] R. A. DeVore, G. G. Lorentz, Constructive Approximation, Springer-  
804 Verlag, 1991.
- 805 [29] T. W. Roberts, The behavior of flux difference splitting schemes near slowly  
806 moving shock waves, Journal of Computational Physics 90 (1990) 141–160.
- 807 [30] L. R. J., Numerical methods for conservation laws, Basel: Birhauser, Read-  
808 ing, Massachusetts, 1990.

809 **A. Derivation of the entropy residual as a function of density, pres-**  
810 **sure and speed of sound**

The entropy residual is defined as follows:

$$R_{\text{ent}}(\vec{r}, t) = \partial_t s(\vec{r}, t) + \vec{u} \cdot \vec{\nabla} \cdot s(\vec{r}, t),$$

where all variables were defined previously. This form of the entropy residual is not suitable for the low-Mach limit as explained in Section 2.1. In this appendix, we recast the entropy residual  $R_{\text{ent}}(\vec{r}, t)$  as a function of the primitive variables (pressure, velocity and density) and the speed of sound. The first step of this derivation is to use the chain rule, recalling that the entropy is a function of the internal energy  $e$  and the density  $\rho$ , yielding

$$R_{\text{ent}}(\vec{r}, t) = s_e \frac{De}{Dt} + s_\rho \frac{D\rho}{Dt},$$

811 where  $s_e$  denotes the partial derivative of  $s$  with respect to the variable  $e$ . We  
812 recall that  $\frac{D}{Dt}$  denotes the material derivative. Since the internal energy  $e$  is a  
813 function of pressure  $P$  and density  $\rho$  (through the equation of state), we use  
814 again the chain rule to re-express the previous equation as a function of the  
815 material derivatives in  $P$  and  $\rho$ :

$$\begin{aligned} R_{\text{ent}}(\vec{r}, t) &= s_e e_P \frac{DP}{Dt} + (s_e e_\rho + s_\rho) \frac{D\rho}{Dt} \\ &= s_e e_P \left( \frac{DP}{Dt} + \frac{1}{s_e e_P} (s_e e_\rho + s_\rho) \frac{D\rho}{Dt} \right) \\ &= s_e e_P \left( \frac{DP}{Dt} + \left( \frac{e_\rho}{e_P} + \frac{s_\rho}{s_e e_P} \right) \frac{D\rho}{Dt} \right). \end{aligned}$$

To prove that the term multiplying the material derivative of the density is indeed equal to the square of the speed of sound, we recall that the speed of sound is defined as the partial derivative of pressure with respect to density at constant entropy, which can be recast as a function of the entropy as follows (see Appendix A.2 of [14]):

$$c^2 := \left. \frac{\partial P}{\partial \rho} \right|_{s=\text{cst}} = P_\rho - \frac{s_\rho}{s_e} P_e.$$

Using the following relations (see Appendix A.1 of [14])

$$P_e = \frac{1}{e_P} \text{ and } P_\rho = -\frac{e_\rho}{e_P}.$$

Substitution of these expressions into the entropy residual equation above gives Eq. (9), which is recalled below for completeness:

$$R_{\text{ent}}(\vec{r}, t) := \partial_t s + \vec{u} \cdot \vec{\nabla} s = \frac{Ds}{Dt} = \frac{s_e}{P_e} \left( \underbrace{\frac{DP}{Dt} - c^2 \frac{D\rho}{Dt}}_{\tilde{R}_{\text{ent}}(\vec{r}, t)} \right).$$

816 **B. Derivation of the dissipative terms for the Euler equations with**  
817 **variable area using the entropy minimum principle**

818 The Euler equations (without viscous regularization) with variable area are  
819 recalled here

$$\partial_t (\rho A) + \vec{\nabla} \cdot (\rho \vec{u} A) = 0 \quad (43a)$$

$$\partial_t (\rho \vec{u} A) + \vec{\nabla} \cdot [A (\rho \vec{u} \otimes \vec{u} + P \mathbb{I})] = P \vec{\nabla} A \quad (43b)$$

$$\partial_t (\rho E A) + \vec{\nabla} \cdot [\vec{u} A (\rho E + P)] = 0. \quad (43c)$$

822 The specific entropy is a function of the density  $\rho$  and the internal energy  $e$ , i.e.,  
823  $s(e, \rho)$ . The above system of equations satisfies the minimum entropy principle  
824 [30],

$$A \rho \left( \partial_t s + \vec{u} \cdot \vec{\nabla} s \right) \geq 0. \quad (44)$$

825 The entropy function  $s$  satisfies the second law of thermodynamics,  $T ds =$   
826  $de - \frac{P}{\rho^2} d\rho$ , which implies  $s_e := T^{-1}$  and  $s_\rho := -PT^{-1}\rho^{-2}$ . One can show that  
827 [14]

$$s_e = T^{-1} \geq 0 \text{ and } P s_e + \rho^2 s_\rho = 0. \quad (45)$$

828 In order to apply the entropy viscosity method to the variable-area Euler equa-  
829 tions, dissipative terms need to be added to each equation in Eq. (43). The  
830 functional forms of these terms need to be such that the entropy residual de-  
831 rived with these terms present also satisfies the minimum entropy principle. To  
832 prove the minimum entropy principle, the extra terms appearing in the entropy  
833 residual are either recast as conservative terms or shown to be positive. The  
834 rest of this appendix presents this demonstration. Following [14], we first write  
835 the variable-area equations with dissipative terms:

$$\partial_t (\rho A) + \vec{\nabla} \cdot (\rho \vec{u} A) = \vec{\nabla} \cdot f \quad (46a)$$

$$\partial_t (\rho \vec{u} A) + \vec{\nabla} \cdot [A (\rho \vec{u} \otimes \vec{u} + P \mathbb{I})] = P \vec{\nabla} A + \vec{\nabla} \cdot g \quad (46b)$$

$$\partial_t (\rho E A) + \vec{\nabla} \cdot [\vec{u} A (\rho E + P)] = \vec{\nabla} \cdot (h + \vec{u} \cdot g). \quad (46c)$$

838 where  $f$ ,  $g$  and  $h$  are dissipative fluxes to be determined. Starting from the  
839 modified system of equations given in Eq. (46), the entropy residual is derived  
840 again. The derivation requires the following steps : express the governing laws  
841 in terms of primitive variables  $(\rho, \vec{u}, e)$ , multiply the continuity equation by  $\rho s_\rho$   
842 and the internal energy equation by  $s_e$ , and invoke multivariate chain rule, e.g.,  
843  $\partial s / \partial x = s_e \partial e / \partial x + s_\rho \partial \rho / \partial x$ . These steps are similar to those used for the  
844 standard Euler equations [14]. Some of the lengthy algebra is omitted here.  
845 The above steps yield:

$$A \rho \left( \partial_t s + \vec{u} \cdot \vec{\nabla} s \right) = s_e \left[ \vec{\nabla} \cdot h + g : \vec{\nabla} u + \left( \frac{u^2}{2} - e \right) \vec{\nabla} \cdot f \right] + \rho s_\rho \vec{\nabla} \cdot f. \quad (47)$$

846 The next step consists of choosing a definition for each of the dissipative terms  
 847 so that the left hand-side is positive. The right hand-side of Eq. (47) can be  
 848 simplified using the relations  $g = A\mu\vec{\nabla}^s\vec{u} + f \otimes \vec{u}$  and  $h = \tilde{h} - 0.5\|\vec{u}\|^2 f$  to give

$$A\rho\left(\partial_t s + \vec{u} \cdot \vec{\nabla} \cdot s\right) = s_e \left[\vec{\nabla} \cdot \tilde{h} - e\vec{\nabla} \cdot f\right] + \rho s_\rho \vec{\nabla} \cdot f + A s_e \mu \vec{\nabla}^s \vec{u} : \vec{\nabla} \vec{u}. \quad (48)$$

The right hand-side is now integrated by parts:

$$A\rho\left(\partial_t s + \vec{u} \cdot \vec{\nabla} \cdot s\right) = \vec{\nabla} \cdot \left[s_e \tilde{h} - s_e e f + \rho s_\rho f\right] \\ - \vec{\nabla} \cdot \tilde{h} \vec{\nabla} s_e + f \cdot \vec{\nabla} (e s_e) - f \cdot \vec{\nabla} (\rho s_\rho) + A s_e \mu \vec{\nabla}^s \vec{u} : \vec{\nabla} \vec{u} \quad (49)$$

849 where  $\vec{\nabla}^s$  is the symmetric gradient. The term  $A s_e \mu \vec{\nabla}^s \vec{u} : \vec{\nabla} \vec{u}$  is positive and  
 850 thus, does not need any further modification. It remains to treat the other  
 851 terms of the right hand-side that we now call *rhs*:

$$rhs = \vec{\nabla} \cdot \left[s_e \tilde{h} - s_e e f + \rho s_\rho f\right] - \tilde{h} \cdot \vec{\nabla} s_e + f \cdot \vec{\nabla} (e s_e) - f \cdot \vec{\nabla} (\rho s_\rho).$$

852 The first term in *rhs* is a conservative term. By carefully choosing a definition  
 853 for  $\tilde{h}$  and  $f$ , the conservative term can be expressed as a function of the entropy  
 854  $s$ . The inclusion of the variable area in the choice of the dissipative terms is also  
 855 required so that, when assuming constant area, the standard Euler equations  
 856 are recovered. The following definitions for  $\tilde{h}$  and  $f$  are chosen:

$$\tilde{h} = A\kappa\vec{\nabla}(\rho e) \text{ and } f = A\kappa\vec{\nabla}\rho,$$

857 which yields, using the chain rule,

$$rhs = \vec{\nabla} \cdot (\rho A\kappa\vec{\nabla}s) - A\kappa \underbrace{\left[\vec{\nabla}(\rho e)\vec{\nabla}s_e - \vec{\nabla}\rho\vec{\nabla}(e s_e) + \vec{\nabla}\rho\vec{\nabla}(\rho s_\rho)\right]}_{\mathbf{Q}}$$

858 It remains to treat the term  $\mathbf{Q}$  that can be recast under a quadratic form.  
 859 Following [14], one obtain:

$$\mathbf{Q} = \rho X^t \Sigma X \\ \text{with } X = \begin{bmatrix} \vec{\nabla}\rho \\ \vec{\nabla}e \end{bmatrix} \text{ and } \Sigma = \begin{bmatrix} \rho^{-2}\partial_\rho(\rho^2\partial_\rho s) & \partial_{\rho,e}s \\ \partial_{\rho,e}s & \partial_{e,e}s \end{bmatrix}$$

860 The matrix  $\Sigma$  is symmetric and identical to the matrix obtained in [14]. The sign  
 861 of the quadratic form can be simply determined by studying the positiveness of  
 862 the matrix  $\Sigma$ . In this particular case, it is required to prove that the matrix is  
 863 negative definite: the quadratic form is on the right hand-side and is preceded by  
 864 a negative sign. According to [14], the convexity of the opposite of the entropy  
 865 function, i.e.,  $-s$ , with respect to the internal energy  $e$  and the specific volume  
 866  $1/\rho$  is sufficient to ensure that the matrix  $\Sigma$  is negative definite.  
 867 Thus, the right hand-side of the entropy residual Eq. (47) is now either recast  
 868 as conservative terms, or known to be positive. Thus, the entropy minimum  
 869 principle holds.



### 870 **C. Entropy residual for isentropic flows**

871 This appendix shows that the entropy residual is zero for isentropic flows.  
 872 For convenience, we recall here the entropy residual as a function of the pressure,  
 873 density, velocity, and speed of sound:

$$\tilde{R}_{\text{ent}} = \frac{DP}{Dt} - c^2 \frac{D\rho}{Dt}. \quad (50)$$

874 Assuming an isentropic flow, pressure is only a function of density, i.e.,  $P =$   
 875  $f(\rho)$  or equivalently  $\rho = f^{-1}(P)$ . Using the definition of the speed of sound  
 876  $c^2 = \left. \frac{\partial P}{\partial \rho} \right|_s$  and the above form of the equation of state, we have

$$c^2 = \left. \frac{\partial P}{\partial \rho} \right|_s = \frac{dP}{d\rho} = \frac{df(\rho)}{d\rho}. \quad (51)$$

877 Using the chain rule, the entropy residual in Eq. (50) can be recast as follows  
 878 and proven equal to zero:

$$\tilde{R}_{\text{ent}} = \frac{df(\rho)}{d\rho} \frac{D\rho}{Dt} - c^2 \frac{D\rho}{Dt} = c^2 \frac{D\rho}{Dt} - c^2 \frac{D\rho}{Dt} = 0. \quad (52)$$